The Malina oceanographic expedition: How do changes in ice cover, permafrost and UV radiation impact biodiversity and biogeochemical fluxes in the Arctic Ocean?

Philippe Massicotte[1], Rainer Amon[2,3], David Antoine[4,5], Philippe Archambault[6], Sergio Balzano[7,8,9], Simon Bélanger[10], Ronald Benner[11,12], Dominique Boeuf[7], Annick Bricaud[5], Flavienne Bruyant[1], Gwenaëlle Chaillou[13], Malik Chami[14], Bruno Charrière[15], Jingan Chen[16], Hervé Claustre[5], Pierre Coupel[1], Nicole Delsaut[15], David Doxaran[5], Jens Ehn[17], Cédric Fichot[18], Marie-Hélène Forget[1], Pingqing Fu[19], Jonathan Gagnon[1], Nicole Garcia[20], Beat Gasser[21], Jean-François Ghiglione[22], Gaby Gorsky[5], Michel Gosselin[13], Priscillia Gourvil[23], Yves Gratton[24], Pascal Guillot[13], Hermann J. Heipieper[25], Serge Heussner[15], Stanford B. Hooker[26], Yannick Huot[27], Christian Jeanthon[7], Wade Jeffrey[28], Fabien Joux[22], Kimitaka Kawamura[29], Bruno Lansard[30], Edouard Leymarie[5], Heike Link[31], Connie Lovejoy[1], Claudie Marec[1,32], Dominique Marie[7], Johannie Martin[1], Guillaume Massé[1,33], Atsushi Matsuoka[1], Vanessa McKague[34], Alexandre Mignot[5,35], William L. Miller[36], Juan-Carlos Miquel[21], Alfonso Mucci[37], Kaori Ono[38], Eva Ortega-Retuerta[22], Christos Panagiotopoulos[20], Tim Papakyriakou[17], Marc Picheral[5], Dieter Piepenburg[39,40], Louis Prieur[5], Patrick Raimbault[20], Joséphine Ras[5], Rick A. Reynolds[41], André Rochon[13], Jean-François Rontani[20], Catherine Schmechtig[42], Sabine Schmidt[43], Richard Sempéré[20], Yuan Shen[11,44], Guisheng Song[45,46], Dariusz Stramski[41], Dave Stroud G.[47], Eri Tachibana[38], Alexandre Thirouard[5], Imma Tolosa[21], Jean-Éric Tremblay[1], Mickael Vaïtilingom[48], Daniel Vaulot[7,49], Frédéric Vaultier[20], John K. Volkman[50], Jorien E. Vonk[51], Huixiang Xie[13], Guangming Zheng[41,52,53], and Marcel Babin[1]

[1]Takuvik Joint International Laboratory / UMI 3376, ULAVAL (Canada) - CNRS (France), Université Laval, Québec, QC, Canada
[2]Department of Marine and Coastal Environmental Science, Texas A&M University Galveston Campus, Galveston, Texas, 77553, USA
[3]Department of Oceanography, Texas A&M University, College Station, Texas, 77843, USA
[4]Remote Sensing and Satellite Research Group, School of Earth and Planetary Sciences, Curtin University, Perth, WA 6845, Australia
[5]Sorbonne Université, CNRS, Laboratoire d'Océanographie de Villefranche (LOV) / UMR 7093, F-06230 Villefranche-sur-Mer, France
[6]ArcticNet, Québec-Océan, Takuvik Joint International Laboratory / UMI 3376, ULAVAL (Canada) - CNRS (France), Université Laval, Québec, QC, Canada
[7]Sorbonne Université, CNRS, Station Biologique de Roscoff - Adaptation et Diversité en Milieu Marin / UMR 7144, 29680 Roscoff, France
[8]Present address: Stazione Zoologica Anton Dohrn Napoli (SZN), Naples, Italy
[9]NIOZ Royal Netherlands Institute for Sea Research, Den Burg, Netherlands
[10]Département de Biologie, Chimie et Géographie (groupes BORÉAS et Québec-Océan), Université du Québec à Rimouski, Rimouski, QC, Canada
[11]School of the Earth, Ocean and Environment, University of South Carolina, Columbia, South Carolina, 29208, USA

[12]Department of Biological Sciences, University of South Carolina, Columbia, South Carolina, 29208, USA

[13]Québec-Océan, Institut des sciences de la mer de Rimouski (ISMER), Université du Québec à Rimouski, Rimouski, QC, Canada

[14]Sorbonne Université, CNRS, Laboratoire Atmosphères Milieux Observations Spatiales (LATMOS) / UMR 8190, Boulevard de l'Observatoire, CS 34229, 06304 Nice Cedex, France

[15]Université de Perpignan Via Domitia (UPVD), CNRS, Centre de Formation et de Recherche sur les Environnements Méditerranéens (CEFREM) / UMR 5110, 52 Avenue Paul Alduy, 66860 Perpignan Cedex, France

[16]SKLEG, Institute of Geochemistry, Chinese Academy of Sciences, 99 West Lincheng Road, Guiyang, Guizhou 550081, P.R. China

[17]Centre for Earth Observation Science, Department of Environment and Geography, University of Manitoba, Winnipeg, MB, Canada

[18]Department of Earth and Environment, Boston University, Boston, Massachusetts, 02215, USA

[19]Institute of Surface-Earth System Science, Tianjin University, Tianjin, China

[20]Aix Marseille Université, Université de Toulon, CNRS, IRD, Mediterranean Institute of Oceanography (MIO) UM 110, 13288 Marseille, France

[21]International Atomic Energy Agency (IAEA) / Environment Laboratories, MC98000, Monaco, Monaco

[22]Sorbonne Université, CNRS, Laboratoire d'Océanographie Microbienne (LOMIC) / UMR 7621, Observatoire Océanologique de Banyuls, France

[23]Sorbonne Université, CNRS, Station Biologique de Roscoff - Centre de recherche et d'enseignement en biologie et écologie marines / FR2424, 29680 Roscoff, France

[24]Institut national de la recherche scientifique - Centre Eau Terre Environnement (INRS-ETE), Québec, QC, Canada

[25]Department of Environmental Biotechnology, Helmholtz Centre for Environmental Research - UFZ, Permoserstraße 15, D-04318 Leipzig, Germany

[26]Ocean Ecology Laboratory, NASA Goddard Space Flight Center, Greenbelt, MD, United States

[27]Département de géomatique appliquée, Université de Sherbrooke, Sherbrooke, QC, Canada

[28]Center for Environmental Diagnostics & Bioremediation, Universty of West Florida, 11000 University Parkway, Pensacola, FL 32514 USA

[29]Chubu Institute for Advanced Studies, Chubu University, Kasugai, Japan

[30]IPSL and Université Paris-Saclay, CEA-CNRS-UVSQ, Laboratoire des Sciences du Climat et de l'Environnement (LSCE) / UMR 8212, 91190 Gif-sur-Yvette, France

[31]Department Maritime Systems, University of Rostock, 18059 Rostock, Germany

[32]Université de Bretagne Occidentale - UBO, CNRS, IRD, Institut Universitaire Européen de la Mer (IUEM) / UMS 3113, 29280 Plouzané, France

[33]Station Marine de Concarneau, MNHN-CNRS-UPMC-IRD, Laboratoire d'océanographie et du climat : expérimentations et approches numériques (LOCEAN) / UMR 7159, 29900 Concarneau, France

[34]Center for Marine and Environmental Studies, University of the Virgin Islands, St. Thomas, VI, USA

[35]Mercator Ocean International, Parc Technologique du Canal, 8-10 rue Hermès – Bâtiment C, 31520 Ramonville Saint-Agne, France

[36]Department of Marine Sciences, University of Georgia, 325 Sanford Dive, Athens, GA 30602

[37]GEOTOP and Department of Earth and Planetary Sciences, McGill University, Montréal, QC, Canada

[38]Institute of Low Temperature Science, Hokkaido University, Sapporo, 060-0819, Japan

[39]Alfred Wegener Institute, Helmholtz Centre for Polar and Marine Research, Am Handelshafen 12, 27570 Bremerhaven, Germany

[40]Helmholtz Institute for Functional Marine Biodiversity at the University of Oldenburg, Ammerländer Heerstraße 231, 26129 Oldenburg, Germany

[41]Marine Physical Laboratory, Scripps Institution of Oceanography, University of California San Diego, La Jolla, CA, USA

[42]Sorbonne Université, CNRS, Ecce Terra Observatoire des Sciences de l'Univers (OSU) - UMS 3455, 4, Place Jussieu 75252 Paris Cedex 05, France

[43]Université de Bordeaux, CNRS, OASU, Environnements et Paléoenvironnements Océaniques et Continentaux (EPOC) / UMR 5805, F-33615 Pessac, France
[44]State Key Laboratory of Marine Environmental Science, College of Ocean and Earth Sciences, Xiamen University, Xiamen, Fujian, P. R. China
[45]Institut des sciences de la mer de Rimouski (ISMER), Université du Québec à Rimouski, Rimouski, QC, Canada
[46]School of Marine Science and Technology, Tianjin University, Tianjin, 300072, China
[47]Department of Physics, Ohio State University, Columbus, Ohio 43210, USA
[48]Université des Antilles Pointe-à-Pitre, Laboratoire de Recherche en Géosciences et Energies (LARGE) / EA 4539, Guadeloupe, France
[49]Asian School of the Environment, Nanyang Techonological University, Singapore
[50]CSIRO Marine and Atmospheric Research and CSIRO Wealth from Oceans Nationa lResearch Flagship, GPO Box 1538, Hobart, Tasmania 7001, Australia
[51]Department of Earth Sciences, Vrije Universiteit Amsterdam, The Netherlands
[52]NOAA/NESDIS Center for Satellite Applications and Research, 5830 University Research Court, College Park, MD 20740, USA
[53]Earth System Science Interdisciplinary Center, University of Maryland Research Park, 5825 University Research Court, College Park, MD 20740, USA

Correspondence: Marcel Babin (marcel.babin@takuvik.ulaval.ca)

Abstract. The MALINA oceanographic campaign was conducted during summer 2009 to investigate the carbon stocks and the processes controlling the carbon fluxes in the Mackenzie River estuary and the Beaufort Sea. During the campaign, an extensive suite of physical, chemical and biological variables was measured across seven shelf–basin transects (south-north) to capture the meridional gradient between the estuary and the open ocean.

5   Key variables such as temperature, absolute salinity, radiance, irradiance, nutrient concentrations, chlorophyll-a concentration, bacteria, phytoplankton and zooplankton abundance and taxonomy, and carbon stocks and fluxes were routinely measured onboard the Canadian research icebreaker *CCGS Amundsen* and from a barge in shallow coastal areas or for sampling within broken ice fields. Here, we present the results of a joint effort to tidy and standardize the collected data sets that will facilitate their reuse in further studies of the changing Arctic Ocean. The

10   dataset is available at https://doi.org/10.17882/75345 (Massicotte et al., 2020).

1   Introduction

The Mackenzie River is the largest source of terrestrial particles entering the Arctic Ocean (see Doxaran et al. (2015) and references therein). During the past decades, temperature rise, permafrost thawing, coastal erosion, and increasing river runoff have contributed to intensifying the export of terrestrial carbon by the Mackenzie River to the

15   Arctic Ocean (e.g. Tank et al. (2016)). Furthermore, the environmental changes currently happening in the Arctic may have profound impacts on the biogeochemical cycling of this exported carbon. On one hand, reduction in sea-ice extent and thickness expose a larger fraction of the ocean surface to higher solar radiations and increase the mineralization of this carbon into atmospheric CO_2 through photo-degradation (Miller and Zepp, 1995; Bélanger

et al., 2006). On the other hand, the possible increase in nutrients brought by Arctic rivers may contribute to higher
20 autotrophic production and sequestration of organic carbon (Tremblay et al., 2014).

Given that these production and removal processes are operating simultaneously, the fate of arctic river carbon transiting toward the Arctic Ocean is not entirely clear. Hence, detailed studies about these processes are needed to determine if the Arctic Ocean will become a biological source or a sink of atmospheric CO_2. With regard to this question, the MALINA oceanographic expedition was designed to document and get insights on the stocks and the
25 processes controlling carbon fluxes in the Mackenzie River and the Beaufort Sea. Specifically, the main objective of the MALINA oceanographic expedition was to determine how (1) primary production, (2) bacterial activity and (3) organic matter photo-oxidation influence carbon fluxes and cycling in Canadian Beaufort Sea. In this article, we present an overview of an extensive and comprehensive data set acquired from a coordinated international sampling effort conducted in the Mackenzie River and in the Beaufort Sea in August 2009.

30 **2 Study area, environmental conditions and sampling strategy**

2.1 Study area and environmental conditions

The MALINA oceanographic expedition was conducted between 2009-07-30 and 2009-08-25 in the Mackenzie River and the Beaufort Sea systems (Fig. 1). The Mackenzie River Basin is the largest in northern Canada and covers an area of approximately 1 805 000 km^2, which represents around 20% of the total land area of Canada (Abdul Aziz and
35 Burn, 2006). Between 1972 and 2016, the average monthly discharge (recorded at the Arctic Red River station) varied between 3296 and 23241 m^3 s^{-1} (shaded area in Fig. 2A). The period of maximum discharge usually occurs at the end of May with decreasing discharge until December, whereas the period of low and stable discharge extends between December and May. During the MALINA oceanographic cruise, the daily discharge varied between 12600 and 15100 m^3 s^{-1} (red segment in Fig. 2A, see also Ehn et al. (2019)). Draining a vast watershed, the Mackenzie River annually
40 delivers on average 2100 Gg C yr^{-1} and 1400 Gg C yr^{-1} of particulate organic carbon (POC) and dissolved organic carbon (DOC), respectively, into the Arctic Ocean (Stein and Macdonald, 2004; Raymond et al., 2007). During the expedition conducted onboard the CCGS Amundsen, the air temperature recorded by the foredeck meteorological tower varied between -2 and 11 °C (Fig. 2B). The average air temperature was 3 °C and usually remained above 0 °C.

2.2 General sampling strategy

45 The sampling was conducted over a network of sampling stations organized into seven transects identified with three digits: 100, 200, 300, 400, 500, 600 and 700 (Fig. 1A). Stations were sampled across the seven shelf–basin transects (south-north) to capture the meridional gradient between the estuary and the open ocean (except for transect 100 across the mouth of the Amundsen Gulf). Within each transect, station numbers were listed in descending order from south to north. Because our goal was to sample in open waters, the order in which the transects were visited
50 depended on the ice cover. The shelf region was not ice-free before mid-August. The bathymetry at the sampling

stations varied between 2 and 1847 m (394 ± 512 m, mean ± standard deviation). The stations in the Beaufort Sea were sampled onboard the Canadian research icebreaker *CCGS Amundsen*. Biological, chemical and optical water column sampling was almost always restricted to the first 400 m of the water column during daytime. Deeper profiles for sampling the whole water column and bottom sediment were usually repeated during nighttime at the same stations. Sediment sampling for fauna and biogeochemistry was conducted at eight stations (110, 140, 235, 260, 345, 390, 680, 690). Two transects (600 and 300) were extended to very shallow waters on the shelf and sampled from either a zodiac or a barge (the bathymetry profiles are shown in Fig. 1B). In the context of this data paper, these two transects were chosen to present an overview of the principal variables measured during the MALINA campaign. A summary of the various sampling strategies is presented below.

2.3 CTD and rosette deployment

Onboard the *CCGS Amundsen*, a General Oceanic rosette equipped with a CTD (Seabird SBE-911+) was deployed at each sampling station (Fig. 1). The rosette was equipped with twenty-four 12-L Niskin bottles. The rosette was also equipped with a transmissometer sensor (WetLabs), a PAR sensor (Biospherical), an oxygen sensor (SBE-43), a pH sensor (SBE-18), a nitrate sensor (Satlantic ISUS), a fluorometer (Sea Point) and an altimeter (Benthos). A surface PAR (Biospherical) was also installed on the roof of the rosette control laboratory. A 300 kHz, downward-looking L-ADCP (Lowered Acoustic Doppler Current Profiler) and a UVP5 (Underwater Vision Profiler, Hydroptics) were also mounted on the rosette frame providing size and abundance of particles above 200 µm and plankton above 700 µM. The Rosette data processing and quality control are described in detail in Guillot and Gratton (2010). Data processing included the following steps: validation of the calibration coefficients, conversion of data to physical units, alignment correction and extraction of useless data. Oxygen sensor calibration was done using Winkler titrations and salinity data were compared with water samples analyzed with a Guideline 8400B Autosal. The quality control tests were based on the International Oceanographic Commission suggested procedures and the UNESCO's algorithm standards (Commission of the European Community, 1993). The recorded data were averaged every decibar. The L-ADCP data were processed according to Visbeck (2002). On August 5th, the pH sensor was replaced by a chromophoric dissolved organic matter (CDOM) fluorometer (Excitation: 350-460 nm/emission 550 nm HW 40 nm; Dr. Haardt Optik Mikroelektronik). The rosette depth range was restricted to the first 1000 m when carrying the pH, PAR and nitrates sensors because of their rating.

3 Data quality control and data processing

Different quality control procedures were adopted to ensure the integrity of the data. First, the raw data were visually screened to eliminate errors originating from the measurement devices, including sensors (systematic or random) and errors inherent from measurement procedures and methods. Statistical summaries such as average,

standard deviation and range were computed to detect and remove anomalous values in the data. Then, data were checked for duplicates and remaining outliers. The complete list of variables is presented in Table 1.

4 Data description: an overview

85 The following sections present an overview of a subset of selected variables. For these selected variables, a brief description of the data collection methods is presented along with general results.

4.1 Water masses distribution

According to previous studies (Carmack et al., 1989; Macdonald et al., 1989), five main source-water types can be distinguished in the southeastern Beaufort Sea : (1) meteoric water (MW, Mackenzie River plus precipitation), (2)
90 sea-ice meltwater (SIM), (3) winter polar mixed layer (wPML), (4) upper halocline water (UHW, modified Pacific Water with core salinity of 33.1 PSU), (5) and lower halocline water (LHW, water of Atlantic origin). In this study, we used the optimum multiparameter (OMP) algorithm to quantify the relative contributions of the different source water types to the observed data (https://omp.geomar.de/). We used salinity, TA, and δ^{18}O as conservative tracers as well as temperature and O_2 concentration as non-conservative tracers, to constrain the water mass analysis, following
95 Lansard et al. (2012). Briefly, the method finds the best fitting fraction (x) of ($n+1$) source water types that contribute to the (n) observed values of the selected tracers in a parcel of water via a solution of an overdetermined system of linear equations that minimizes the residual error. Boundary conditions were applied to the method to guarantee that all fractions calculated were positive and that the sum of all fractions was 100% (mass conservation).

During MALINA, the Mackenzie Shelf was entirely ice-free, and the ice-pack was located beyond the shelf break.
100 The transition zone was characterized by different expanses of drifting sea-ice. Significant contributions of Meteoric Water (> 25%) to the surface mixed layer (SML) were only observed close to the Mackenzie River mouth and on the inner shelf (Fig. 3). A relatively small fraction of sea-ice meltwater was detected beyond the shelf break, mostly along the transect 600. Below the SML, the wPML was the predominant water mass down to 100 m depth. The UHW extends from the interior ocean onto the outer shelf from 120 to 180 m of depth. Relatively high fractions
105 of UHW were also found at 50 m depth along the Mackenzie and Kugmallit Canyons, which are recognized sites of enhanced shelf-break upwelling caused by wind- and ice-driven ocean surface stresses. Below 200 m depth, the LHW with an Atlantic origin was always the prevailing water mass.

4.2 Temperature and salinity from the CTD

Temperature and salinity for the first 100 m of transects 600 and 300, the two transects originating from the Macken-
110 zie delta, are presented in Fig. 4. They confirm what was found by the water mass analysis (section 4.1): most of the freshwater is coming from the western part of the Mackenzie delta. This is also in accordance with many studies that documented that during the summer, a combination of ice melting and river runoff was generating a highly strat-

ified surface layer (Carmack and Macdonald, 2002; Forest et al., 2013). The signature of an eddy may be observed at 75 m in the salinity data at 70 °N, approximately 70 km from shore (Fig. 4B).

4.3 Underwater bio-optical data

4.3.1 Inherent Optical Properties (IOPs) profiling from the ship, the barge and the zodiac

The total, non-water, spectral absorption (a), attenuation (c) and backscattering coefficients (b_b) were measured using a AC9 attenuation and absorption meter and a BB9 scattering meter (WetLabs), a HydroScat-6P and a-Beta sensors (HOBI Labs) either attached to the CTD-Rosette frame onboard the *CCGS Amundsen* or deployed separately from the barge or the Zodiac tender. These devices were using either 10 cm or 25 cm optical path lengths, depending on the turbidity of the water sampled. Detailed information about the deployment and the data processing of the IOP data can be found in Doxaran et al. (2012).

Fig. 5 shows cross-sections of the total absorption and backscattering coefficients at 440 nm ($a(440)$ and $b_b(440)$) derived as $b_b = b_{bp} + b_{bw}$, where b_{bw} is the backscattering coefficient of pure seawater (Morel, 1974). Both $a(440)$ and $b_b(440)$ showed the same patterns along the transects 600 and 300. Close to the estuary, higher absorption (Fig. 5A) and total scattering (Fig. 5B) can be observed at the surface, likely reflecting the important quantities of dissolved and particulate organic matter delivered by the Mackenzie River. Higher values are also observed in transect 600 compared to transect 300, which is further away from the mouth of the Mackenzie River. Both $a(440)$ and $b_b(440)$ decreased rapidly toward higher latitudes where the water of the Mackenzie River mixes with seawater from the Beaufort Sea.

4.3.2 Particulate and CDOM absorption

Chromophoric dissolved organic matter absorption (a_{CDOM}) was measured from water samples filtered with 0.2 μm GHP filters (Acrodisc Inc.), using an UltraPath (World Precision Instruments Inc.) between 200 and 735 nm. In most cases, a 2 meters optical path length was used for the measurement, except for coastal waters near the Mackenzie River mouth (Fig. 1) where a 0.1 meters optical path length was used. Particulate absorption (ap) was measured using a filter-pad technique modified from Röttgers and Gehnke (2012). Briefly, sea-water was filtered through a 25 mm Whatman GF/F (glass-fiber filters) less than 3h after sampling. Filters were placed in the center of a 150 mm integrating sphere equipped with a handmade Spectralon filter holder. The spectral optical density ($\text{OD}(\lambda)$) of the particles retained on the filter was then measured using a PerkinElmer Lambda-19 spectrophotometer, from 300–800 nm at 1nm resolution. More details about particulate and dissolved absorption measurements can be found in Röttgers and Gehnke (2012), Bélanger et al. (2013) and Matsuoka et al. (2012).

Examples of a_{CDOM} spectra measured at the surface for the northernmost and the southernmost stations of transects 600 and 300 are presented in Fig. 6A. The marked influence of the organic matter of terrestrial origin can be observed for the stations located at the mouth of the Mackenzie River (697 and 398). Because the organic matter

145 delivered by the river is highly humic and coloured, the absorption at 254 nm was approximately 15 times higher at the southern shelf stations for both transects compared to the northern stations (620 and 320). Likewise, the specific UV absorbance of dissolved organic carbon at 254 nm (SUVA$_{254}$), a metric commonly used as a proxy for assessing both chemical (Weishaar et al., 2003; Westerhoff et al., 2004) and biological reactivity (Berggren et al., 2009; Asmala et al., 2013) of the DOM pool in natural aquatic ecosystems, decreased rapidly along the south-north gradient in both

150 transects 600 and 300 (Fig. 6C). This observation is in accordance with a previous study that showed that SUVA$_{254}$ was higher in inland ecosystems due to elevated lateral connectivity with surrounding terrestrial landscape and organic matter inputs from the tributaries (Massicotte et al., 2017). The decrease in SUVA$_{254}$ toward north stations (Fig. 6C) suggests that terrestrially-derived DOM transiting toward the ocean is gradually degraded into smaller and more refractory molecules.

155 Particulate absorption spectra (a_p) for the northernmost and the southernmost stations of transects 600 and 300 are presented in Fig. 6B. Particulate absorption at the stations located in the estuary (697 and 398) was much higher than that measured at the open water stations (620 and 320). For instance $a_p(443)$ measured at stations 620 (0.03 m^{-1}) and 697 (8.62 m^{-1}), the northernmost and the southernmost stations of transects at the mouth of the Mackenzie River, shows that ap decreases rapidly along the latitudinal axes. This can be possibly explained

160 because the drained organic and inorganic material from the surrounding landscape of the Mackenzie's watershed is degraded or sediment rapidly as it is transferred to the ocean.

4.3.3 Other optical measurements and radiometric quantities

Other optical instruments were attached to the rosette sampler. These include a transmissometer (Wetlabs C-Star, path 25 cm) for beam attenuation measurement, a chlorophyll fluorometer (SeaPoint) and a CDOM fluorometer

165 (Optic & Mikro-elektonik, Germany, see Amon et al. (2003)). Additionally, a LISST-100X (Laser In Situ Scattering and Transmissometry, Sequoia Scientific) was attached to the rosette and provided beam attenuation (532 nm) and forward light scattering measurements at 32 angles from which particle size distribution was estimated. Various optical measurements were also made in the laboratory to determine other IOPs. These include the absorption of coloured dissolved (a_{CDOM}) and particulate (a_p) organic matter, the absorption coefficients of non-algal particles

170 (a_{NAP}) and phytoplankton (a_{phi}). Apparent optical properties (AOPs) measurements included light transmittance (T), photosynthetically available radiation (PAR), downward irradiance (E_d), upwelled radiance (L_u) and global solar irradiance (E_s). The latter three radiometric quantities were measured simultaneously using a Compact-Optical Profiling System (C-OPS) manufactured by Biospherical Instruments Inc. (San Diego, California) that was deployed during MALINA Leg2b. The principal data products obtained from the C-OPS data were the diffuse attenuation

175 coefficient (K_d) plus the water-leaving radiance (L_W) including all normalized forms. Detailed methodology and results derived from C-OPS measurements can be found in Doxaran et al. (2012), Antoine et al. (2013), Bélanger et al. (2013) and Hooker et al. (2013).

4.4 Nutrients

Samples for nitrate, nitrite, soluble reactive phosphorus and silicate determination were collected into 20 mL polyethy-
180 lene flasks, immediately poisoned with mercuric chloride (Kirkwood, 1992), and stored for subsequent laboratory
analysis according to Raimbault et al. (1990) and Aminot and Kérouel (2007). Ammonium concentrations (40 mL col-
lected into 60 mL polycarbonate tubes) were measured onboard using the sensitive method of Holmes et al. (1999)
having a detection limit of 5 nmoles L^{-1}. Samples for organic matter determination were collected into 50-mL Glass
Schott bottles, immediately acidified with 100 µl of 0.5N H_2SO_4 and stored in the dark at 5 °C. Dissolved organic
185 carbon (DOC), dissolved organic nitrogen (DON) and dissolved organic phosphorus (DOP) were determined at the
laboratory using the wet-oxidation procedure according to Raimbault et al. (1999a).

Nitrate levels were always very low at the surface, with concentration generally lower than 0.01 µmoles L^{-1}, except
in the Mackenzie plume (Fig. 7). It is interesting to note that nitrate was never entirely depleted, and some traces
(0.005 to 0.01 µmoles L^{-1}) were always detectable in surface waters (Fig. 7A). Ammonium distribution showed the
190 same pattern. Even if concentrations were very low (generally < 0.03 µmoles L^{-1}), this nutrient, like nitrate, was
always detected, suggesting that in situ sources of nitrate and ammonium exist offshore, certainly due to biological
processes. Phosphate concentrations showed the opposite distribution (Fig. 7B). Despite nitrogen depletion, surface
waters were always phosphate replete. Highest concentrations, around 0.5 µmoles L^{-1}, were observed far from
Mackenzie's mouth, revealing a clear west-east gradient. The silicate distribution was similar to that of nitrate. But
195 Surface waters were always silicate-repleted with concentrations largely above the detection limit (> 4 µmoles L^{-1}).
The impact of the Mackenzie River was clear, close to the coast for inorganic nutrients and farther offshore for
dissolved organic nutrients. A quarter of the estimated annual nutrient supply by the Mackenzie River occurred
during July-August. The supply of DON was eight times larger than that of nitrate-N. By contrast, the amount of
DOP supplied was only 2.5 times higher than the amount of phosphate (Tremblay et al., 2014). The Mackenzie River
200 enriched the western Canadian Beaufort Shelf with inorganic and organic N, potentially supporting most of the
primary production, but not with phosphate or ammonium. Large deliveries of N relative to P by rivers relax coastal
communities from N limitation, allowing them to tap into the excess P originating from the Pacific Ocean. Then,
river inputs locally rectified the strong regional deficit of inorganic N, i.e. negative N* (Tremblay et al., 2014).

4.5 Dissolved Organic Carbon (DOC), Total Dissolved Nitrogen (TDN), Total Hydrolyzable Amino Acids
205 (THAA), and Total Dissolved Lignin Phenols (TDLP$_9$)

Water samples were collected at selected stations and water masses for analyses of dissolved organic carbon (DOC),
total dissolved nitrogen (TDN), total hydrolyzable amino acids (THAA), and total dissolved lignin phenols (TDLP$_9$)
concentrations. Samples for DOC, TDN, and THAA were gravity-filtered from Niskin bottles using pre-combusted
glass-fibre (GF/F) filters (0.7 µm pore size) and stored frozen (-20 °C) immediately after collection in pre-combusted
210 borosilicate glass vials (Shen et al., 2012). Samples for TDLP$_9$ analysis (between 1 and 10 L) were gravity-filtered

from Niskin bottles using Whatman Polycap AS cartridges (0.2-µm pore size), acidified to pH between 2.5 and 3 with sulfuric acid and extracted within a few hours using C-18 cartridges (Louchouarn et al., 2000; Fichot et al., 2013). The C-18 cartridges were stored at 4 °C until elution with 30 mL of methanol (HPLC-grade), and the eluent was stored in sealed, pre-combusted glass vials at -20 °C until analysis. DOC and TDN concentrations were measured

215   by high-temperature combustion using a Shimadzu total organic carbon analyzer (TOC-V) equipped with an inline chemiluminescence nitrogen detector and an autosampler (Benner and Strom, 1993). Blanks were negligible and the coefficient of variation between injections of a given sample was typically < 1%. Analysis of a deep seawater reference standard (University of Miami) every sixth sample was used to check the accuracy and consistency of measured DOC and TDN concentration. Total hydrolyzable amino acids (THAA) were determined as the sum of 18

220   dissolved amino acids using an Agilent High-Performance Liquid Chromatography system equipped with a fluorescence detector (excitation: 330 nm; emission: 450 nm). Samples (100 µL) of filtered seawater were hydrolyzed with 6 mol L^{-1} hydrochloric acid using a microwave-assisted vapour phase method (Kaiser and Benner, 2005). Free amino acids liberated during the hydrolysis were separated as o-phthaldialdehyde derivatives using a Licrosphere RP18 or Zorbax SB-C18 column (Shen et al., 2012). Detailed methodological information can be found in Fichot et al. (2013).

225   Surface DOC concentrations along the transects 300 and 600 behaved approximately conservatively with salinity, decreasing from 458 µmol L^{-1} in the Mackenzie River end-member (salinity = 0.2 PSU) to 123 µmol L^{-1} at a salinity of 26.69 PSU (Fig. 8A). DOC concentrations in surface waters further decreased to minimum values of $\approx$ 66 µmol L^{-1} offshore (Fichot and Benner, 2011). Concentrations generally increased by a few µmol L^{-1} in the upper halocline relative to surface values, but then generally decreased with depth, reaching 53-57 µmol L^{-1} in the lower halocline,

230   and $\approx$ 43-50 µmol L^{-1} in deep water-masses (depth > 1000 m). Similar to DOC, surface TDLP$_9$ concentrations along transects 600 and 300 behaved approximately conservatively with salinity, decreasing from $\approx$ 93-96 nmol L^{-1} in the Mackenzie River end-member (salinity = 0.2 PSU) to $\approx$ 12 nmol L^{-1} at a salinity of 26.69 PSU (Fig. 8B). Surface concentrations reached minimum values of $\approx$ 2.5 nmol L^{-1} offshore (Fichot et al., 2016). TDLP$_9$ concentrations generally decreased with depth, reaching minimum values of < 1.5 nmol L^{-1} below the halocline. Surface concentrations of

235   THAA along the transects 600 and 300 decreased from 576 nmol L^{-1} in the Mackenzie River end-member (salinity = 0.2 PSU) to 317 nmol L^{-1} at a salinity of 26.69 PSU (Fig. 8C). Unlike DOC and TDLP$_9$, concentrations of THAA did not follow a conservative mixing line along the salinity gradient. Elevated concentrations of THAA were observed in mid-salinity waters in both transects, suggesting plankton production in these regions. In comparison, THAA concentrations in the slope and basin waters were lower and decreased with depth, reaching minimal values of $\approx$ 70

240   nmol L^{-1} below the halocline (Shen et al., 2012).

4.6   Pigments

Water samples (volumes between 0.25 L and 2.27 L) were filtered through glass fibre GF/F filters (25 mm diameter, particle retention size 0.7 µm). They were immediately frozen at -80 °C, transported in liquid nitrogen, then stored at -80 °C until analysis on land. Samples were extracted in 3 mL HPLC-grade methanol for two hours minimum.

245 After sonication, the clarified extracts were injected (within 24 hours) onto a reversed-phase C8 Zorbax Eclipse column (dimension: 3 x 150 mm, 3.5 µm pore size). The instrumentation comprised an Agilent Technologies 1100 series HPLC system with diode array detection at 450, 667 and 770 nm of phytoplankton pigments (carotenoids, chlorophylls *a*, *b*, *c* and bacteriochlorophyll-*a*). A total of 22 pigments were analyzed and quantified. Details of the HPLC analytical procedure can be found in Ras et al. (2008).

250 As illustrated in Fig. 9, the phytoplankton biomass, indicated by total chlorophyll-*a* concentrations, was the highest at the coast (up to 3.5 mg m^{-3}), decreasing offshore (to about 0.010 mg m^{-3}) with the formation of a Sub-surface Chlorophyll Maximum (SCM) around 60 m. In terms of biomass integrated over the sampled depth, values range from 6.2 and 8.9 mg m^{-2} at the coast to 14.3 and 13.2 mg m^{-2} offshore for transects 300 and 600, respectively. In general, the most predominant accessory pigment was fucoxanthin, indicating that diatoms consti-

255 tute a large proportion of the phytoplankton assemblage. However, in offshore waters and around the SCM, 19'-hexanoyloxyfucoxanthin concentrations were equivalent or sometimes higher than fucoxanthin, suggesting that, in these waters, haptophytes can predominate over diatoms. Other pigments such as chlorophyll-*b* and prasinoxanthin, suggest the presence of green algae, and probably micromonas-type cells, especially in coastal waters and at the surface. For more detailed information, see Coupel et al. (2015) who used this dataset applied to the CHEMTAX

260 (CHEMical TAXonomy) chemotaxonomic tool to assess the distribution of phytoplankton communities.

4.7 Phytoplankton abundance and diversity

The abundance of the eukaryotic pico- and nano-phytoplankton was measured by flow cytometry onboard the Amundsen with a FACS Aria Instrument (Becton Dickinson, San Jose, CA, USA) following the protocol of Marie et al. (1999).

265 In transect 300 and 600 (Fig. 10), the abundance of pico- and nano-phytoplankton reached maximal values around 5000 and 3000 cells mL^{-1} respectively. On transect 600, pico-eukaryotes higher abundances were restricted to the surface layer with a 5 to 10-fold drop at 30 m. In contrast, nano-eukaryotes formed clear deep maxima, especially at stations 610 and 680. On transect 300, pico-eukaryotes were also abundant in the surface at the more off-shore stations. Still, they decreased sharply near-shore, while nano-eukaryotes' highest concentrations were near the river

270 mouth, linked to high diatom concentrations (**?**). The composition of eukaryotic phytoplankton was determined with two different approaches. We isolated 164 cultures using a range of techniques (single-cell isolation, serial dilution, flow cytometry sorting) that have been characterized morphologically and genetically (Balzano et al., 2012, 2017) and deposited to the Roscoff Culture Collection (www.roscoff-culture-collection.org). Among these cultures, several new species have been discovered such as the new species of green algae *Mantoniella beaufortii* (Yau et al., 2020) or the

275 diatom *Pseudo-nitzschia arctica* (Percopo et al., 2016), but more await description in particular among *Pelagophyceae*. One of the strains isolated (RCC2488, *Chlamydomonas malina* nomen nudum) has been recently found to be suitable for biotechnology applications (Morales-Sánchez et al., 2020). We also used molecular approaches by sorting pico- and nano-eukaryotic communities and characterizing their taxonomic composition by TRFLP (terminal-restriction

fragment length polymorphism) analysis and cloning/sequencing of the 18S ribosomal RNA gene (**?**). While the pico-
phytoplankton was dominated by the species *Micromonas polaris*, the nano-phytoplankton was more diverse and
dominated by diatoms mostly represented by *Chaetoceros neogracilis* and *C. gelidus*, with the former mostly present
at surface waters and the latter prevailing in the DCM (**?**). Furthermore, *C. neogracilis* sampled from the Beaufort
Sea consists of at least four reproductively isolated genotypes (Balzano et al., 2017). The comparison between the
taxonomy of natural communities and isolated cultures (Fig. 11) reveals that although we succeeded at isolating
some dominant species in the field such as *M. polaris*, *C. neogracilis* and *C. gelidus* some other important taxa such
as the diatom *Fragiliaropsis* or the haptophyte *Chrysochromulina* were not recovered.

4.8 Carbon fluxes

In the context of climate change, the main objective of the MALINA oceanographic expedition was to determine
how (1) primary production, (2) bacterial activity and (3) photo-degradation influence carbon fluxes and cycling of
organic matter in the Arctic. In the following sections, we present an overview of these processes that are detailed
in Ortega-Retuerta et al. (2012a), Xie et al. (2012), Tremblay et al. (2014) and Link et al. (2013).

4.8.1 Phytoplankton primary production

At each station, when productivity was quantified, rates of carbon fixation (primary production) were determined
using a ^{13}C isotopic technique (Raimbault and Garcia, 2008). For this purpose, three 580 mL samples were collected
at minimum sun elevation or before sunrise at 6-7 depths between the surface and the depth where irradiance was
0.3% of the surface value and poured into acid-cleaned polycarbonate flasks. Incubations were carried out immedi-
ately following the tracer addition in an on-deck incubator. This consisted of 6-7 opaque boxes, each with associated
neutral and blue screens, allowing around 50%, 25%, 15%, 8%, 4%, 1% and 0.3% light penetration. At five stations,
incubations were also performed in situ on a drifting rig with incubation bottles positioned at the same depth where
samples for on-deck incubations were collected. After 24h, samples were filtered through pre-combusted (450 °C)
Whatman GF/F filters (25-mm diameter). After filtration, filters were placed into 2 mL glass tubes, dried for 24h in a
60 °C oven and stored dry until laboratory analysis. These filters were used to determine the final ^{13}C enrichment
ratio in the particulate organic matter on an Integra-CN mass spectrometer. Filtrates were poisoned with $HgCl_2$ and
stored to estimate ammonium regeneration and nitrification rates. The isotopic enrichment of particulate organic
matter and dissolved NH_4+ and NO_3- at the end of incubations were used to calculate net C and N uptake and the
recycling of NH_4+ and NO_3- (Raimbault et al., 1999b).

Daily rates of primary production at the surface were generally very low across the survey area, ranging from 0.1
mg C m^{-3} d^{-1} offshore to a maximum of 545 mg C m^{-3} d^{-1} in Kugmallit Bay (Fig. 12) associated with the Mackenzie
River discharge (Tremblay et al., 2014). Ammonification and nitrification followed the same coastal-offshore pattern
with rates driving most, if not all, of the NH_4+ and NO_3- consumption in the surface layer. Primary production was
generally maximum at the surface, but high rates were often observed at depth in the nitracline layer associated

with a chlorophyll maximum. The range of uptake rates of ammonium in surface generally overlapped with the range of nitrate uptake rates. Nitrate uptake below the surface amounted to 40–60% of total nitrogen uptake, a proportion that is approximately twice greater than at the surface (Ardyna et al., 2017).

315 Nitrification and ammonium regeneration were detectable over the whole water column ranging from 2 to 20 nmoles L^{-1} d^{-1}. The highest rates were generally located at the base of the euphotic zone, leading to the formation of subsurface ammonium and nitrite maximum layers. Surface communities and especially the accumulation of large cells thrived mostly on regenerative NH_4+ and their reliance on NO_3- increased with depth to reach a maximum in the subsurface chlorophyll maximum, where substantial levels of primary production occurred (Ardyna

320 et al., 2017). This is consistent with Ortega-Retuerta et al. (2012a) who reported elevated bacterial abundance and bacterial production rates in association with photoammonification of riverine organic matter (Le Fouest et al., 2013). Nitrification accounted for a variable and sometimes a large share of the NO_3- demand, consistent with the persistence of trace amounts of NO_3- at the surface. Collectively, the data indicate that the coastal Beaufort Sea is an active regenerative system during summer, probably fueled by large pools of organic matter brought by rivers.

325 Consequently, new production was very low and often close to zero in the 0-40 m layer. But high nitrate uptake rates can be observed at depth (Station 135), often associated with high primary production located in the chlorophyll maximum layer being the place of significant new production. The impact of the Mackenzie River on shelf productivity during summer is moderate and associated mostly with localized nutrient recycling in the nearshore estuarine transition zone (Tremblay et al., 2014).

330 ### 4.8.2 Photo-degradation

4.8.2.1 CO and CO_2 production from dissolved organic matter

Surface water samples were gravity-filtered upon collection through a pre-cleaned Pall AcroPak 1000 filtration capsule sequentially containing 0.8 and 0.2 μm polyethersulfone membranes. Filtered water was stored in clear-glass bottles at 4 °C in darkness. CO photoproduction rates (P_{CO}, nmol L^{-1} h^{-1}) were determined aboard the *CCGS Amund-*

335 *sen* immediately after sample collection, whereas CO_2 photoproduction rates (P_{CO2}, nmol L^{-1} h^{-1}) were measured in a land-based laboratory in Rimouski, Québec within three months of sample collection. The sample-pretreatment and irradiation procedures followed those reported previously (Bélanger et al., 2006; Song et al., 2013). Briefly, after minimizing the background CO and CO_2 concentrations, samples were transferred into combusted, quartz-windowed cylindrical cells (CO: i.d.: 3.4 cm, length: 11.4 cm; CO_2: i.d.: 2.0 cm, length: 14 cm) and irradiated at 4 °C

340 using a SUNTEST XLS+ solar simulator equipped with a 1.5-kW xenon lamp. The radiation emitted from the solar simulator was screened with a Schott long-pass glass filter to remove UV radiation < 295 nm. The irradiations lasted for 10 min to 2 h for CO and 24 to 48 h for CO_2. The photon flux reaching the quartz windows of the cells was measured to be 835 μmol m^{-2} s^{-1} for CO and 855 μmol m^{-2} s^{-1} for CO_2 over the wavelength range from 280 to 500 nm.

345   Both P_{CO2} and P_{CO} increased landward, with the difference between the most and least saline samples reaching a factor of ≈ 5 along transect 300 and ≈ 8 along transect 600 for P_{CO2} and of ≈ 7 along transect 600 for P_{CO} (Fig. 13A). This landward increase in P_{CO2} and P_{CO} was due principally to the parallel augmentation in CDOM absorption, as demonstrated by the linear relationships between these two rates with CDOM absorption: $P_{CO2} = 279.1 \times a_{CDOM}(412) - 17.0\,(R^2 = 0.964, n = 9)$ and $P_{CO} = 17.5 \times a_{CDOM}(412) - 4.8\,(R^2 = 0.966, n = 7)$, where $a_{CDOM}(412)$

350   (m^{-1}) is the CDOM absorption coefficient at 412 nm published previously (Song et al., 2013; Taalba et al., 2013). The irradiance-normalized P_{CO2}/P_{CO} ratio gradually decreased landward along transect 600, from 23.5 at station 691 to 16.2 at station 697, suggesting that the near-shore samples were more efficient at CO photoproduction relative to CO_2 photoproduction than the shelf samples. The P_{CO2}/P_{CO} ratios at the two stations on transect 300 were, however, similar (18.9 for station 394 and 20.1 for station 396). Combining the P_{CO2}/P_{CO} ratios from both transects arrives at

355   an average ratio of 19.8 ($\pm$ 2.5 SD), with a rather small relative standard deviation of 12.5%.

It should be pointed out that extrapolating the lab-determined CO_2 and CO photoproduction rates to the sampling area is practically infeasible due to the very different laboratory and real-environmental conditions. For instance, the water column in the Mackenzie estuary and shelf areas contains large amounts of particles (Doxaran et al., 2012), which are also optically active, whereas the irradiated samples were particles-free. Furthermore, the photoproduc-

360   tion rates in the water column would decrease rapidly with depth because of the strong light attenuation by CDOM and particles, while the laboratory radiation at best simulated the radiation of the top 1-2 cm layer of the water column even without considering the constant vs. varying irradiance from the solar simulator and natural sunlight, respectively. To estimate the areal photoproduction rates in the water column from lab-derived data often require coupled optical-photochemical modelling that incorporates spectral apparent quantum yields of the photoproduct

365   of interest (Bélanger et al., 2006; Xie et al., 2009; Fichot and Miller, 2010). Using this approach and CO data from the Malina cruise, Song et al. (2013) estimated a yearly-averaged areal CO photoproduction rate of 9.6 µmol m^{-2} d^{-1} in the Mackenzie estuary and shelf areas, which implies a yearly-averaged areal CO_2 photoproduction rate of 191.1 µmol m^{-2} d^{-1} based on the average P_{CO2}/P_{CO} ratio of 19.8 obtained above. Aggregating the CO_2 and CO rates gives a total photomineralization rate of 199.7 µmol C m^{-2} d^{-1}.

370   **4.8.2.2   Autoxidation of suspended particulate material**

Water samples were filtered immediately after collection through a pre-combusted glass fibre filter (Whatman GF/F, 0.7 µm) under a low vacuum. The filters were frozen immediately at -20 °C until analysis and transported to the laboratory. Treatment of the filters involved $NaBH_{4-}$ reduction and classical alkaline hydrolysis (Rontani et al., 2012). Reduction of labile hydroperoxides to alcohols is essential for estimating the importance of autoxidative degradation

375   in natural samples by gas chromatography-electron impact mass spectrometry (GC-EIMS) (Marchand and Rontani, 2001). Autoxidative degradation of terrigenous particulate organic matter (POM) discharged by the Mackenzie River

was monitored thanks to specific oxidation products of sitosterol (main sterol of higher plants) and dehydroabietic acid (a component of conifers).

380 The autoxidation state of these tracers increases strongly at the offshore stations (Fig. 13B) (reaching 89 and 86% at station 680 and station 380, respectively, in the case of sitosterol, see (Rontani et al., 2014)). These results allowed us to demonstrate that in surface waters of the Beaufort Sea, autoxidation strongly affects vascular plant lipids and probably also the other components of terrestrial OM delivered by the Mackenzie River. Initiation of these abiotic oxidation processes was attributed to the involvement of some enzymes producing radicals (lipoxygenases) present in higher plant debris and whose activity is enhanced at high salinities (Galeron et al., 2018).

385 ### 4.8.2.3 Bacterial production and respiration

Bacterial production (BP, assessed by ^{3}H-leucine incubations, $n = 171$), and respiration (BR, assessed by changes in O_2 by Winkler titration, $n = 13$), were measured from surface waters to 200m waters at 44 sampling locations. Bacterial production ranged from 8.8 to 7078 µg C m^{-3} d^{-1} and showed a marked decreasing pattern from the mouth of the Mackenzie to the open Beaufort Sea and from the surface to deep waters (Fig. 14). Temperature and labile

390 dissolved organic matter (indicated as dissolved amino acids) controlled BP variability (Ortega-Retuerta et al., 2012a), and the nitrogen limitation of surface BP during the summer period was demonstrated experimentally (Ortega-Retuerta et al., 2012b). BR ranged from 5500 to 45500 µg C m^{-3} d^{-1}, leading to a bacterial growth efficiency of 8% on average. BP and BR were low with respect to lower latitudes but within the range of those in polar ecosystems, suggesting the role of low temperatures driving carbon fluxes through bacteria (Kirchman et al., 2009). Bacterial

395 carbon demand (BP + BR), which averaged 21500 ± 14900 µg C m^{-3}, was higher than primary production in the whole study area, indicating that the Mackenzie River platform and the Beaufort Sea are net heterotrophic during summer. This may suggest a temporal decoupling between carbon fixation and remineralization in the area.

4.8.3 Bacterial diversity

Spatial variations in bacterial community structure were explored in surface waters from the Mackenzie River to

400 the open Beaufort Sea ($n = 20$). By using 16S rRNA-based analysis, we investigated both particle-attached (PA, > 3 µm size fraction) and free-living bacteria (FL, size fraction between 3 and 0.2 µm) along a river to open sea transect. Multivariate statistical analysis revealed significant differences in community structure between the river, coastal and open sea waters, mainly driven by salinity, particle loads, chlorophyll-a, and amino acid concentration (Ortega-Retuerta et al., 2013). Bacterial communities differed between PA and FL fractions only in open sea stations, likely

405 due to the higher organic carbon content in particles with respect to particles from the river and coast, which were enriched in minerals. Alphaproteobacteria dominated in FL open sea samples, while the PA fraction was mainly composed of Gammaproteobacteria, Opitutae (Verrucomicrobia) and Flavobacteria. The coastal and river samples were dominated by Betaproteobacteria, Alphaproteobacteria, and Actinobacteria in both the PA and FL fractions

(Fig. 14C). These results highlight the importance of particle quality, a variable that is predicted to change along with
410 global warming, in influencing bacterial community structure, and thus likely altering the biogeochemical cycles that
they mediate.

5 Conclusions

The comprehensive data set assembled during the MALINA oceanographic cruise has given unique insights on the
stocks and the processes controlling carbon fluxes in the Mackenzie River and the Beaufort Sea. In this paper, only
415 a handful of variables have been presented. The reader can find the complete list of measured variables in Table 1,
all of which are also fully available in the data repository. The uniqueness and comprehensiveness of this data set
offer more opportunities to reuse it for other applications.

6 Code and data availability

The raw data provided by all the researchers, as well as metadata, are available on the LEFE-CYBER repository
420 (PROOF / LEFE CYBER CRUISE). The processed and tidied version of the data is hosted at SEANOE (SEA scieNtific Open
data Edition) under the CC-BY license (https://www.seanoe.org/data/00641/75345/, Massicotte et al. (2020)). The raw
UVP5 large particulate data and images are all available from the EcoPart/Ecotaxa website (https://ecotaxa.obs-
vlfr.fr/part/). Detailed metadata are associated with each file, including the principal investigator's contact infor-
mation. For specific questions, please contact the principal investigator associated with the data (see Table 1). The
425 code used to produce the figures and the analysis presented in this paper is available under the GNU GPLv3 licence
(https://doi.org/10.5281/zenodo.4001730).

7   Figures

A
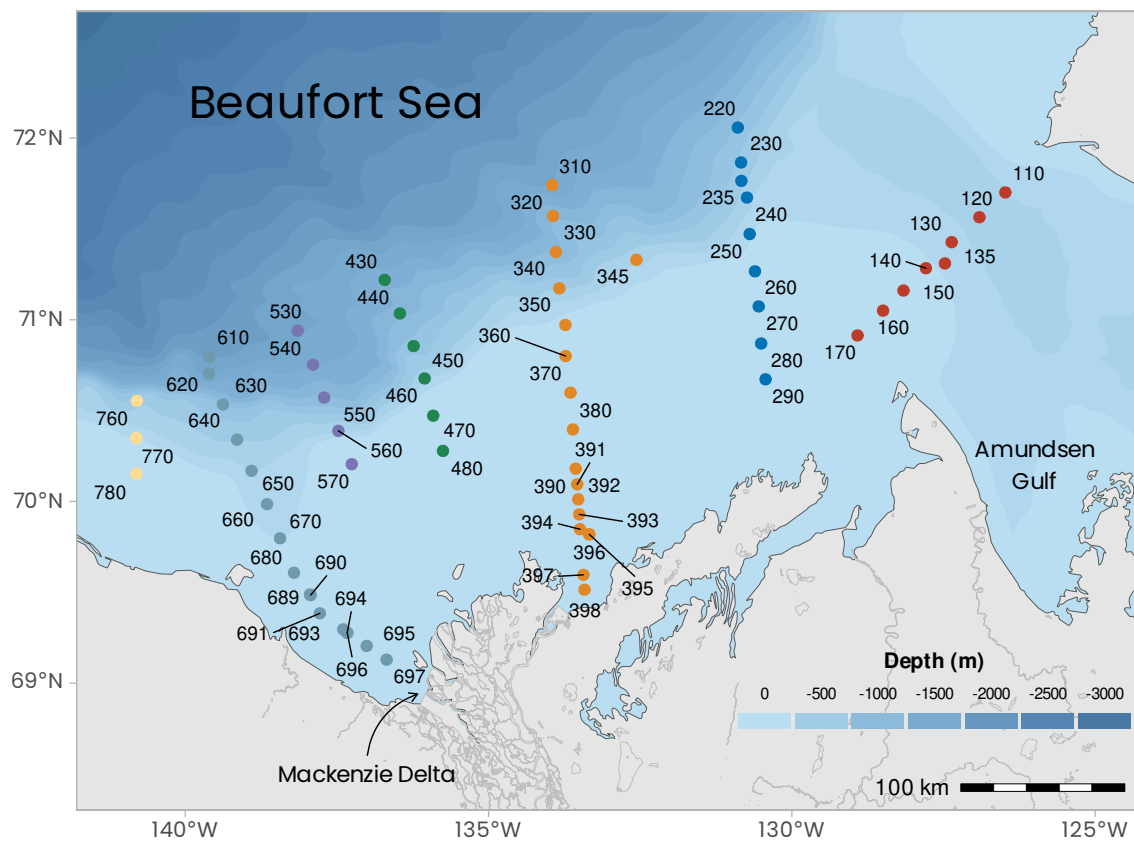
B
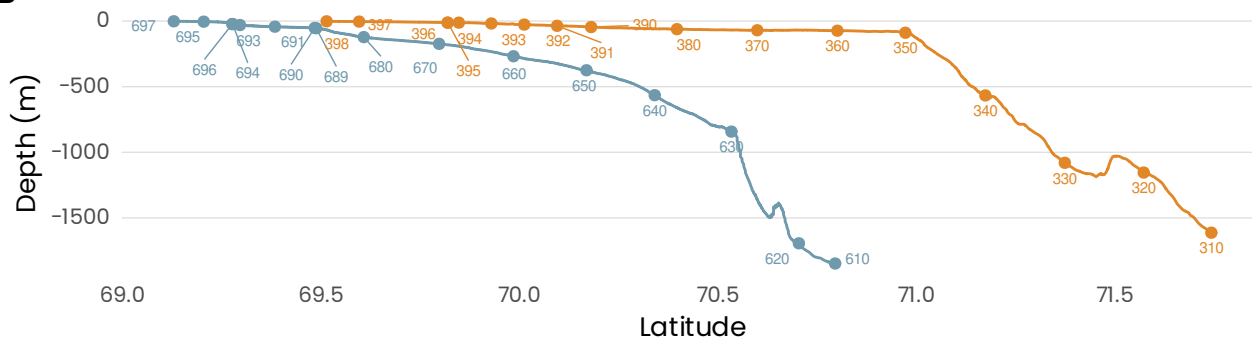
Figure 1. (**A**) Localizations of the sampling sites visited during the MALINA 2009 campaign. The colors of the dots represent the seven transects visited during the mission. (**B**) Bathymetric profiles for transects 600 and 300. Bathymetric data from GEBCO (https://download.gebco.net/).
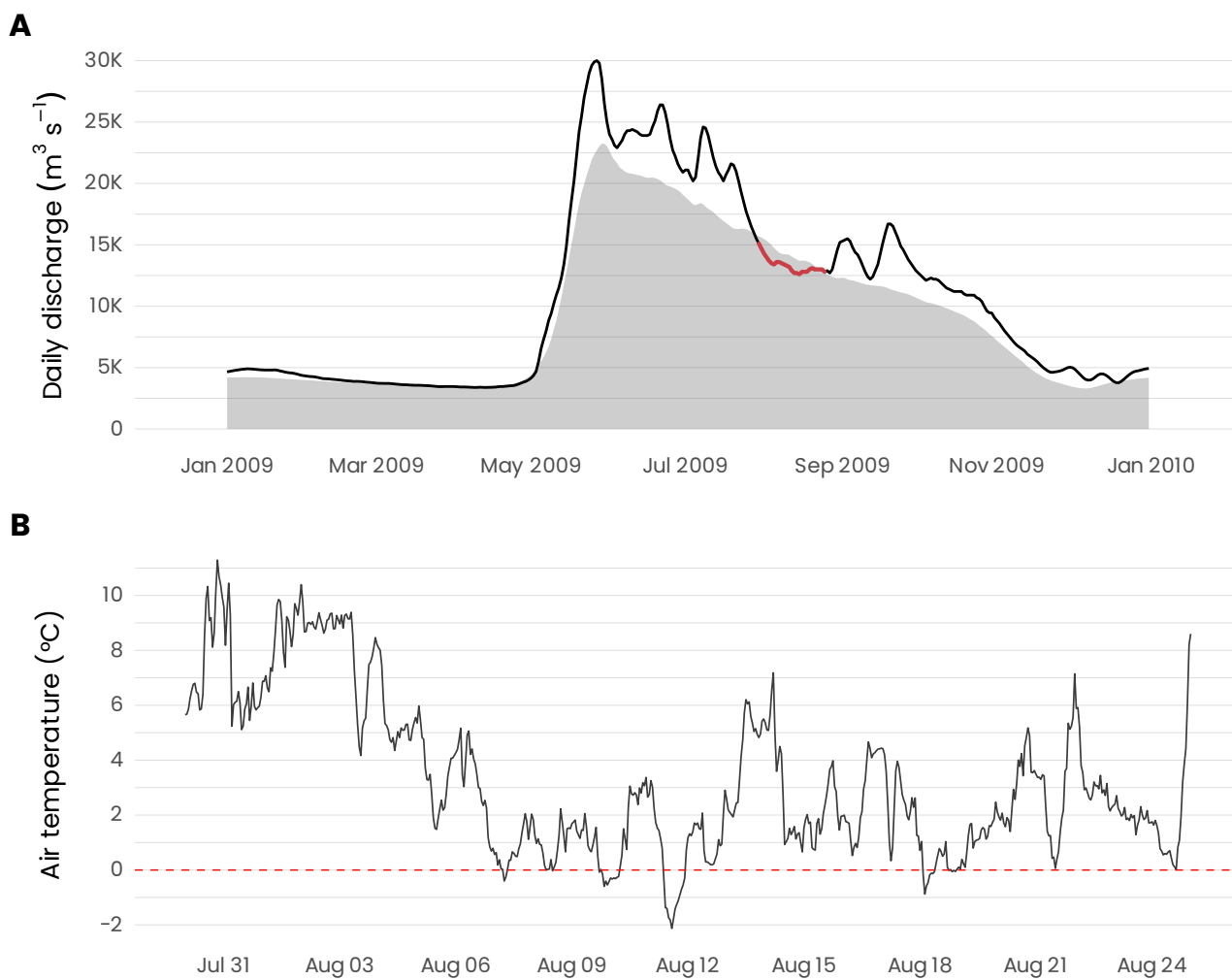
Figure 2. (**A**) Daily discharge of the Mackenzie River at the Arctic Red River junction (station 10LC014). The black line corresponds to the 2009 discharge whereas the coloured segment identifies the period of the MALINA campaign. The shaded area is the mean discharge calculated between 1972 and 2016. Discharge data from the Government of Canada (https://wateroffice.ec.gc.ca/search/historical_e.html). (**B**) Hourly air temperature recorded from the Amundsen's foredeck me-teorological tower during the campaign.
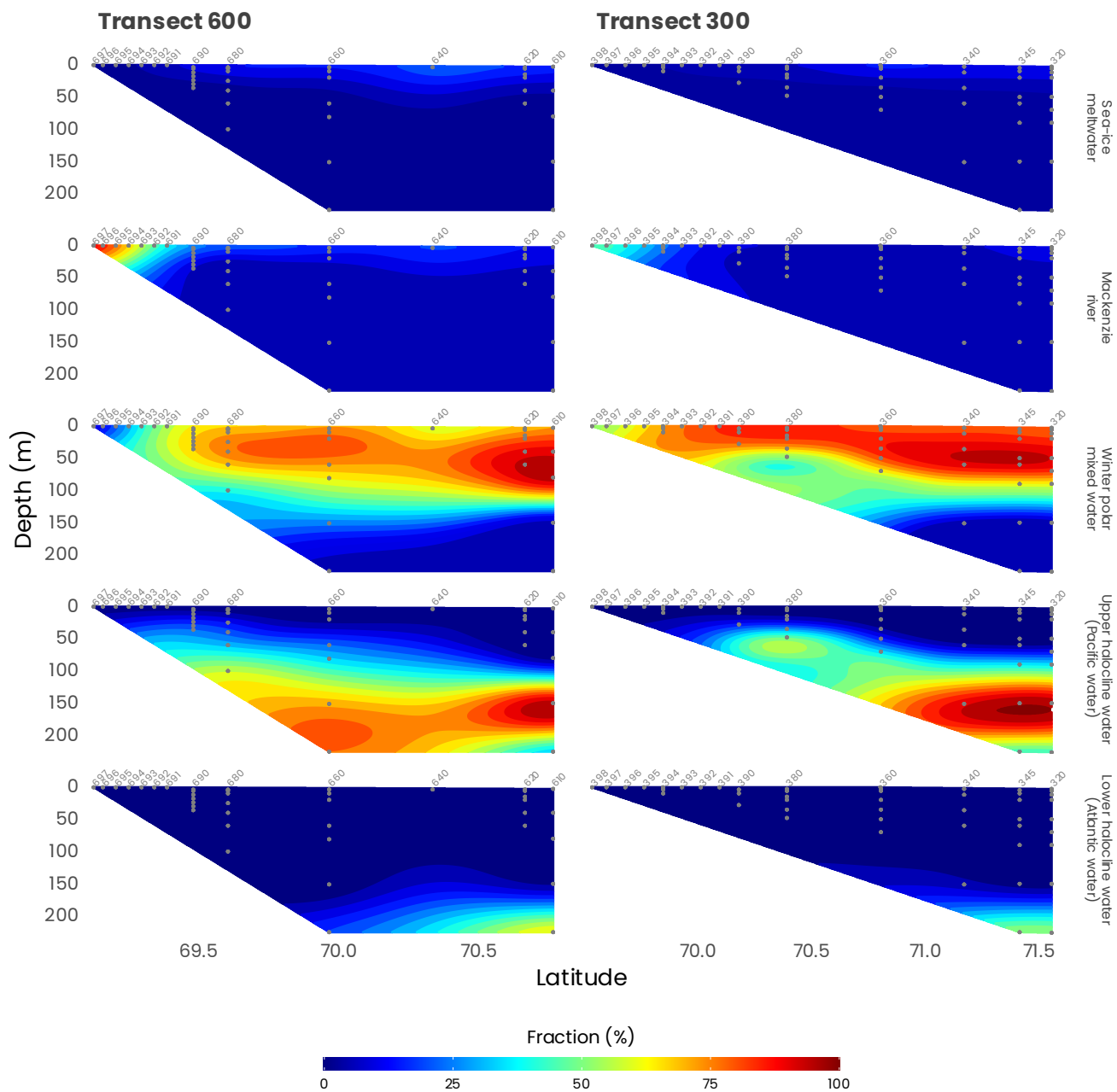
Figure 3. Distribution of source water types along transects 600 and 300 (see Fig. 1). Station numbers are identified in light gray on top of each panel.
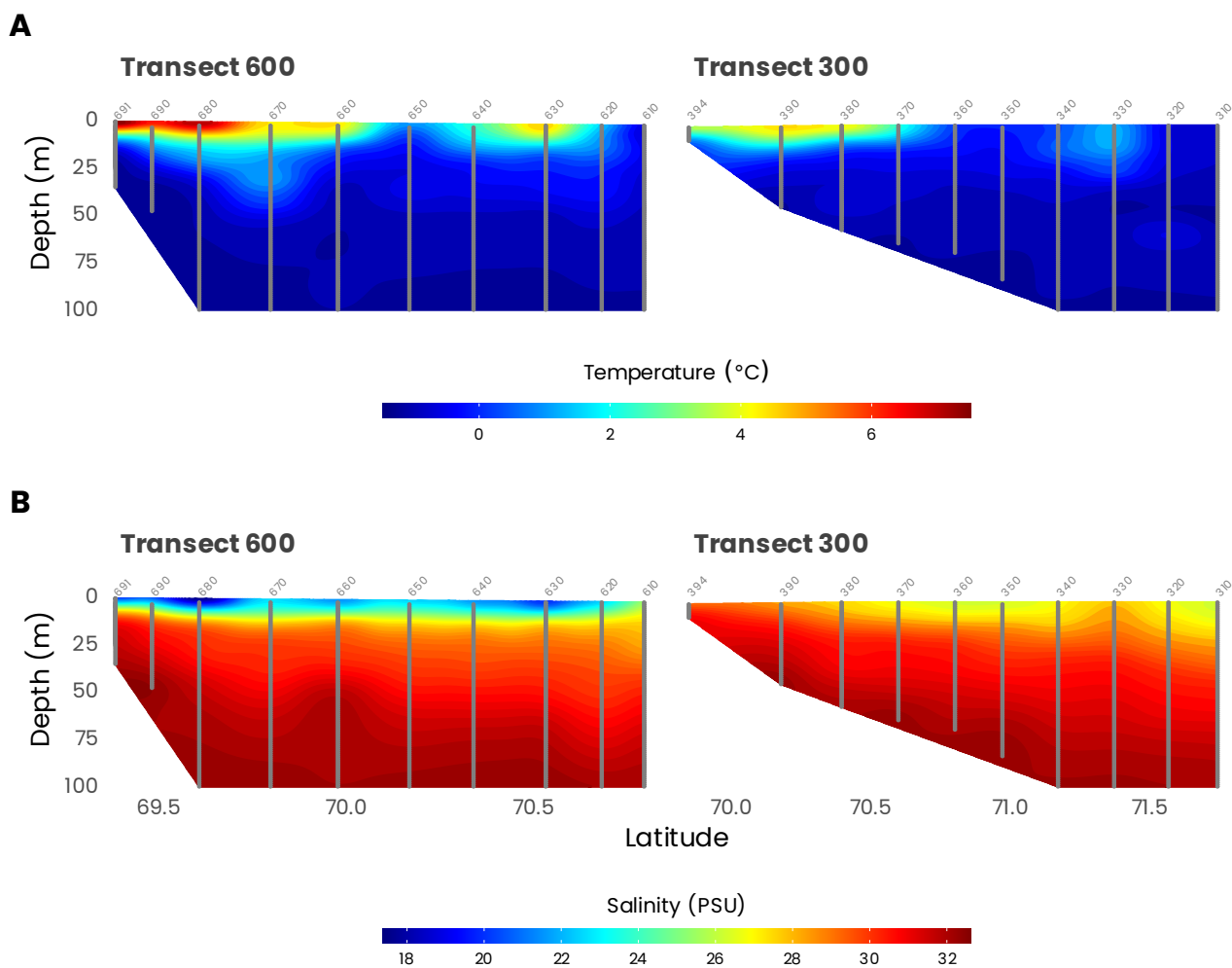
Figure 4. Cross-sections of temperature (**A**) and salinity (**B**) measured by the CTD (gray dots) along transects 600 and 300. Station numbers are identified in light gray on top of each panel.
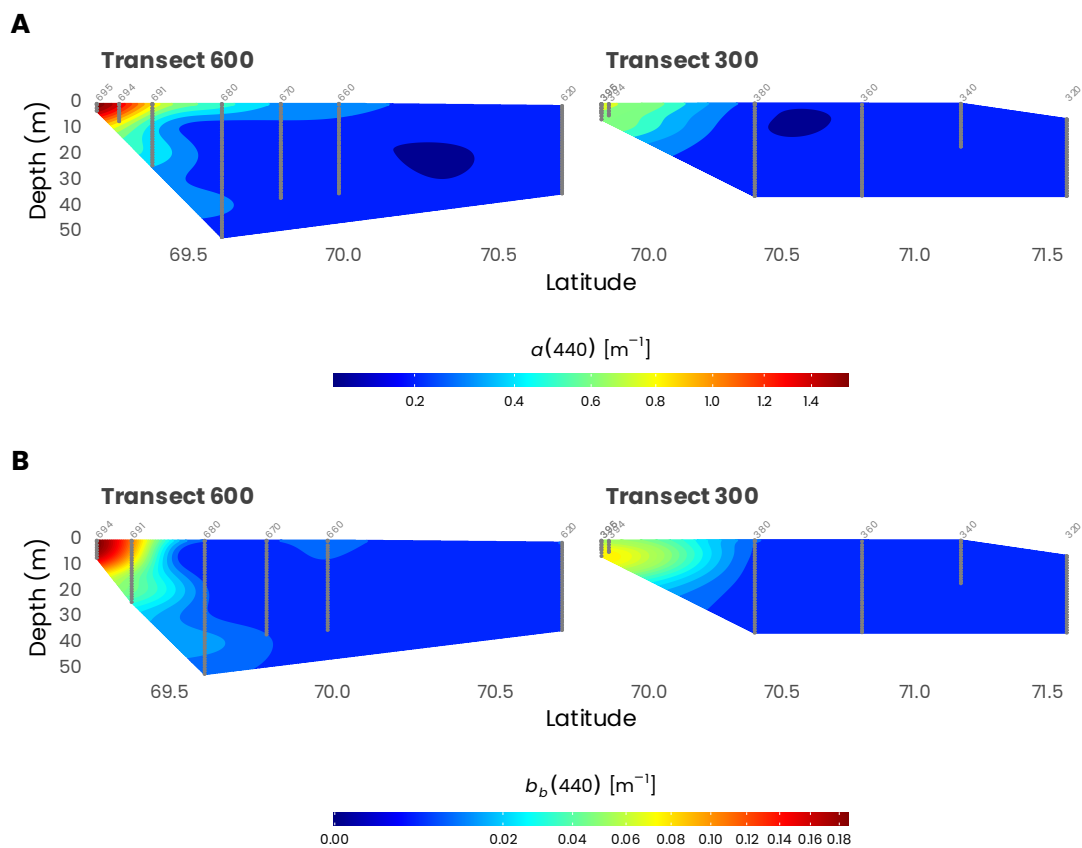
Figure 5. Cross-sections of (**A**) absoprtion ($a(440)$) and (**B**) total scattering ($b_b(440)$) measured from the barge at 440 nm with an AC9 and BB9 respectively along transects 600 and 300. Station numbers are identified in light gray on top of each panel. Note that the data has been square-root transformed for the visualization.
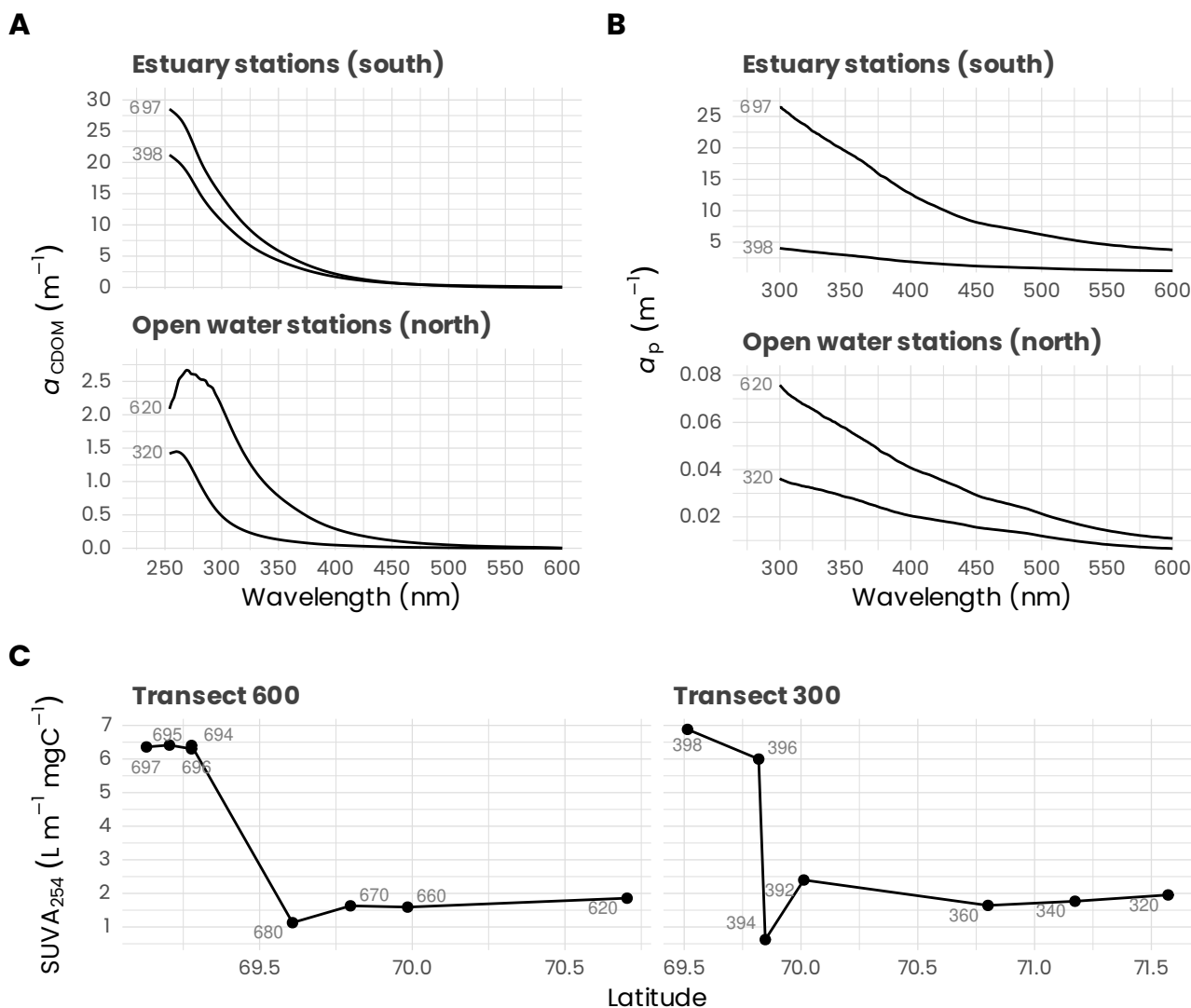
Figure 6. (A) Absorption spectra between 254 and 600 nm of chromophoric dissolved organic matter (a_{CDOM}) measured at the surface for the northern (620, 320) and southern (697, 398) stations of the transects 600 and 300. **(B)** Particulate absorption spectra (a_p) measured between 300 and 600 nm measured at the surface for the northernmost and the southernmost stations of the transects 600 and 300. **(C)** Specific UV absorbance at 254 nm (SUVA$_{254}$, i.e. absorption of light at 254 nm per unit of carbon) at surface for stations along transects 600 and 300. Stations are identified in light gray (see Fig. 1 for an overview of the station locations). Note the difference of the y-axes used in panels A and B which highlight the important differences in dissolved and particulate absorption between stations in the estuary and those offshore.
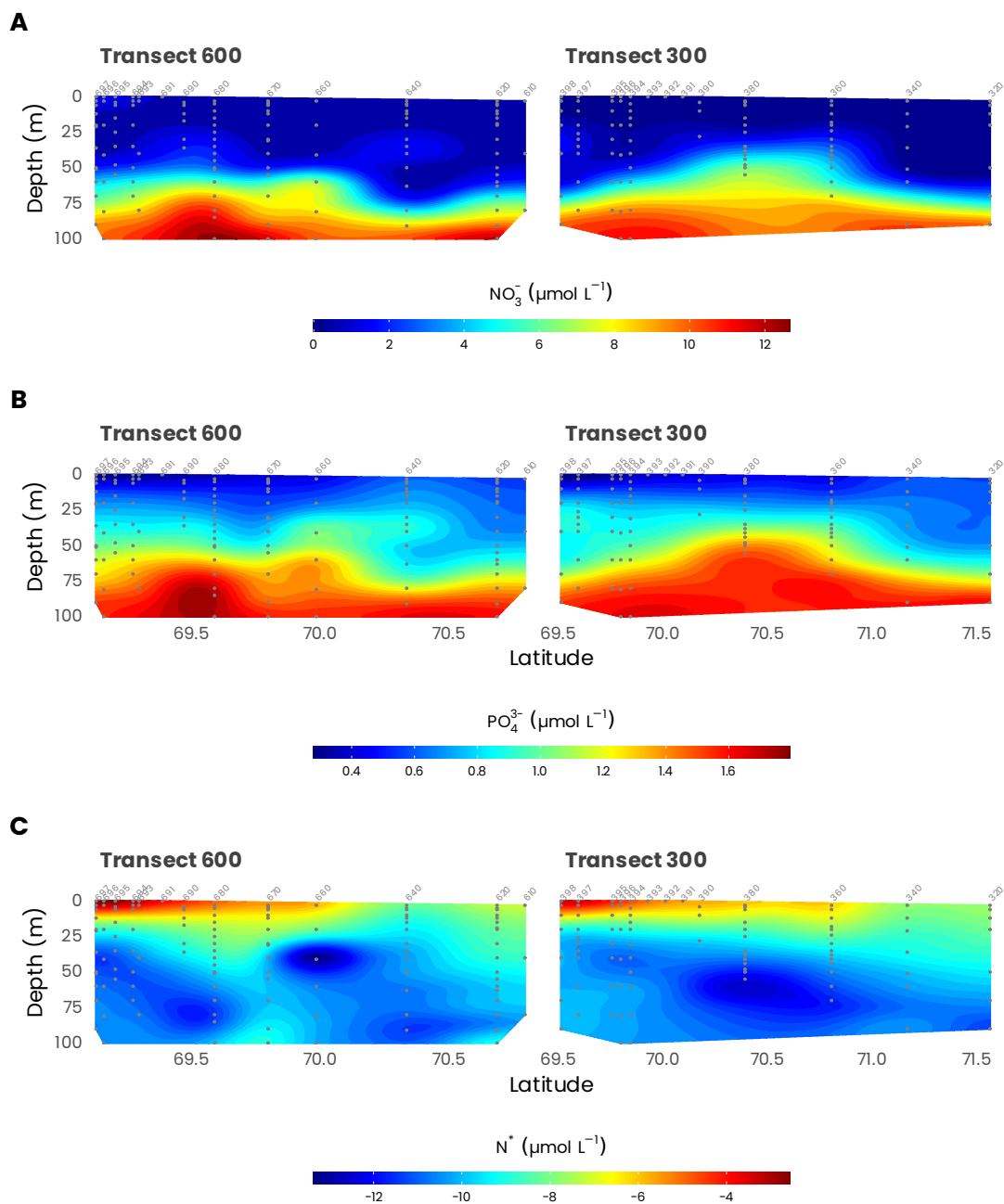
Figure 7. Cross-sections of (**A**) NO_3^- and (**B**) PO_4^{3-} measured from Niskin bottles (gray dots) along transects 600 and 300. (**C**) N* defined as N - rP with r = N/P = 13.1 (see the text for the details). Station numbers are identified in light gray on top of each panel.
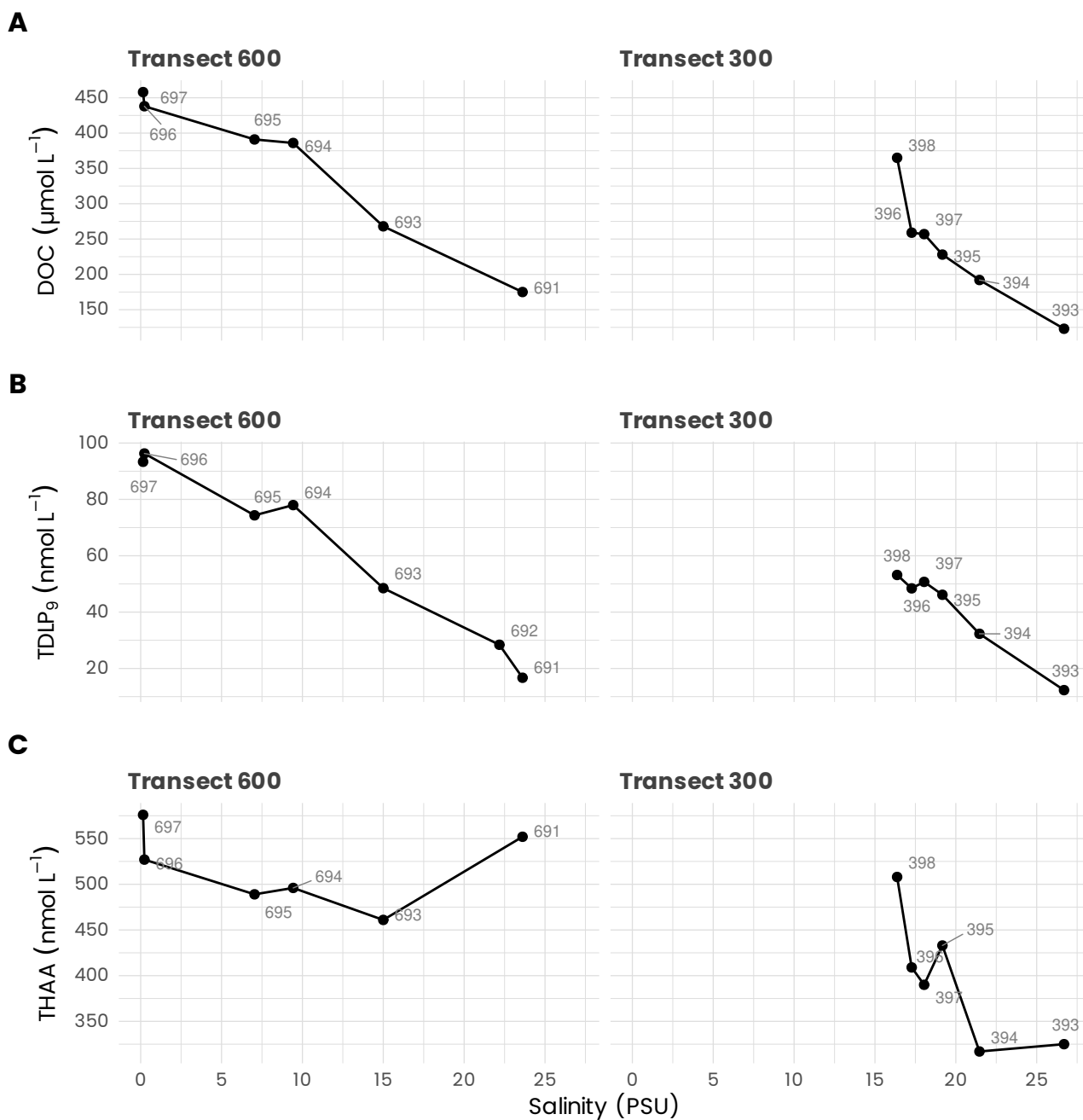
Figure 8. Concentrations of (**A**) dissolved organic carbon (DOC), (**B**) total dissolved lignin phenols (TDLP$_9$), and (**C**) total hydrolysable amino acids (THAA) measured along transects 600 and 300, and plotted against salinity.
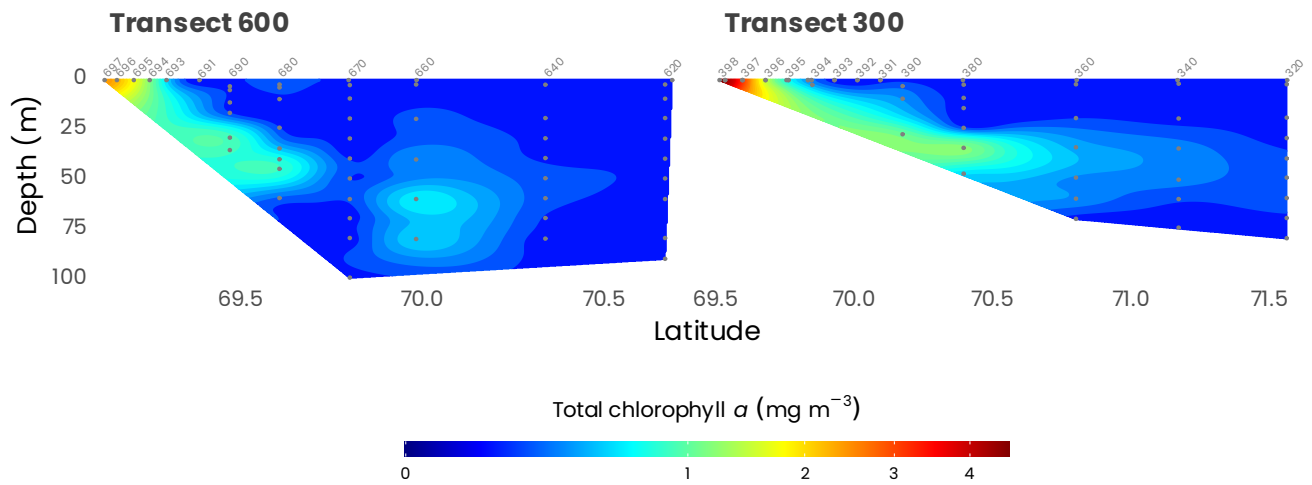
Figure 9. Cross-sections of total chlorophyll-*a* measured from HPLC (gray dots) along transects 600 and 300. Station numbers are identified in light gray on top of each panel. Note that the data has been square-root transformed for the visualization.
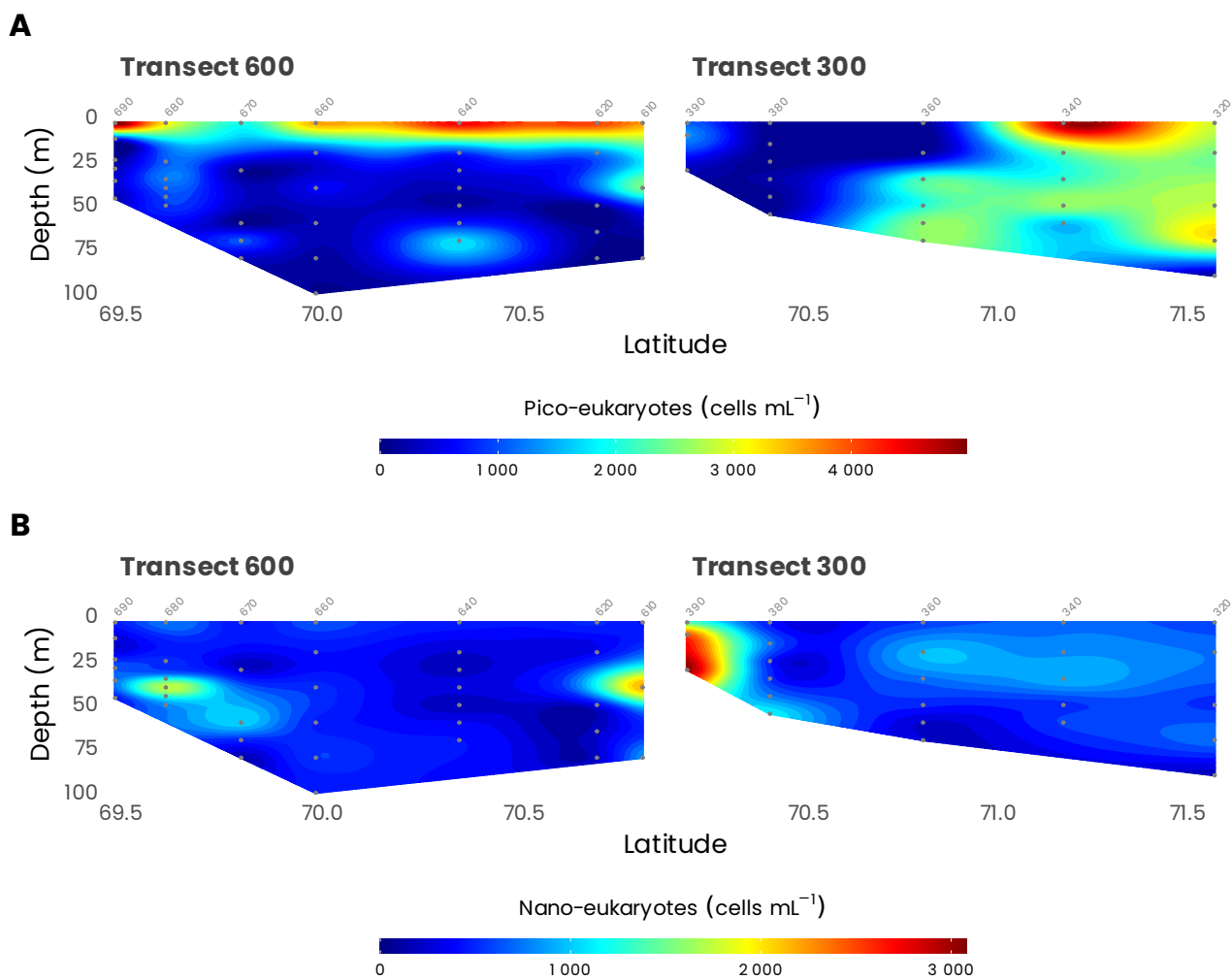
Figure 10. Concentrations of photosynthetic (**A**) pico- and (**B**) nano-eukaryotes measured by flow cytometry during the MALINA cruise on transects 600 and 300.

Figure 11. (**A**) Taxonomic composition of populations of photosynthetic pico- and nano-eukaryotes sorted flow cytometry from clone library sequences (**?**). (**B**) Taxonomic composition of cultures of phytoplankton isolated during the MALINA cruise (Balzano et al., 2012).
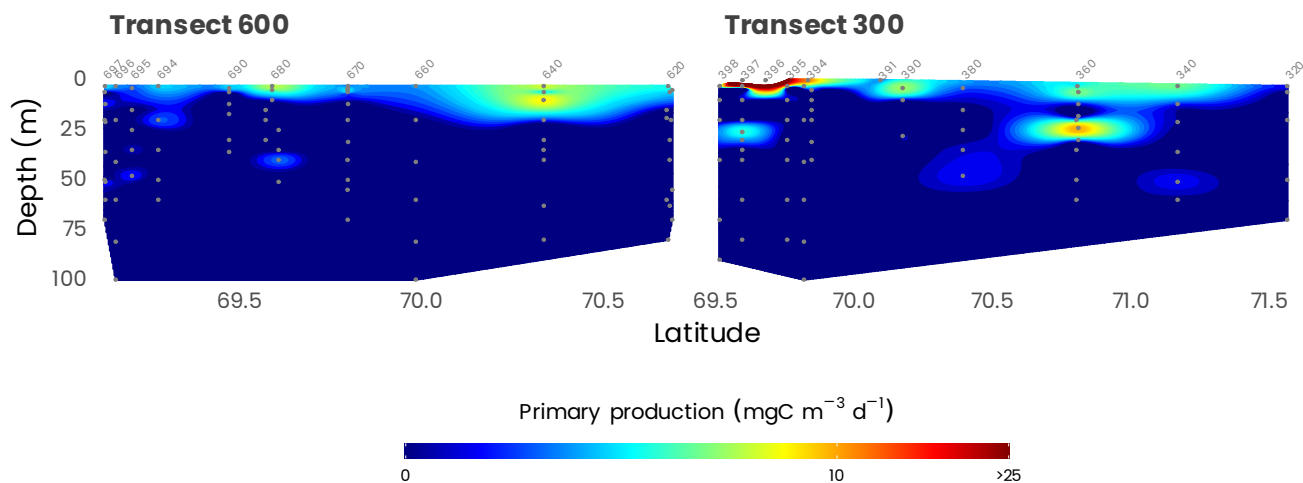
Figure 12. Cross-sections of primary production (gray dots) along transects 600 and 300. Station numbers are identified in light gray on top of each panel. Note that the color scale is presented on a log10 scale.
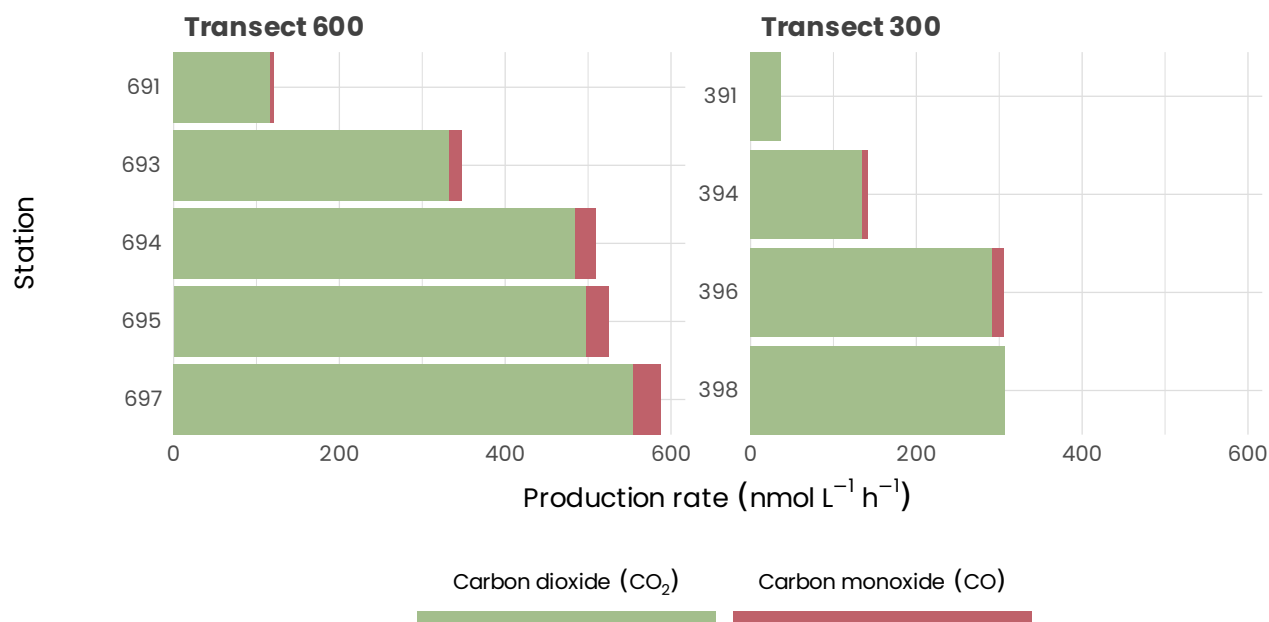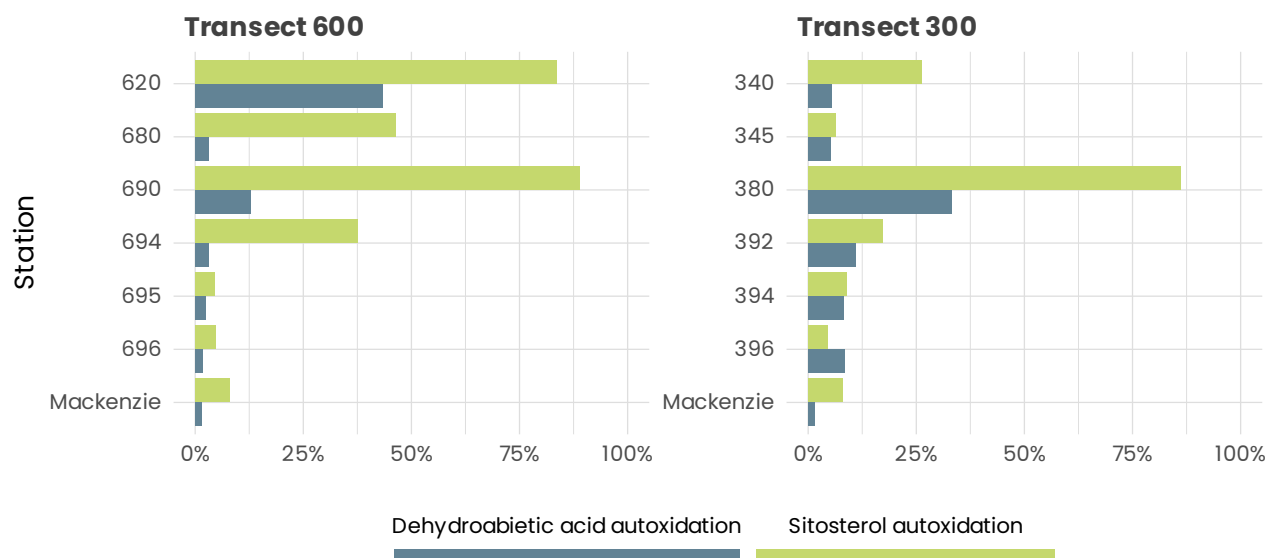
Figure 13. (**A**) CO and CO_2 production measured at 295 nm at surface for stations of transects 600 and 300. (**B**) Autoxidation of suspended particulate material for stations of transects 600 and 300.
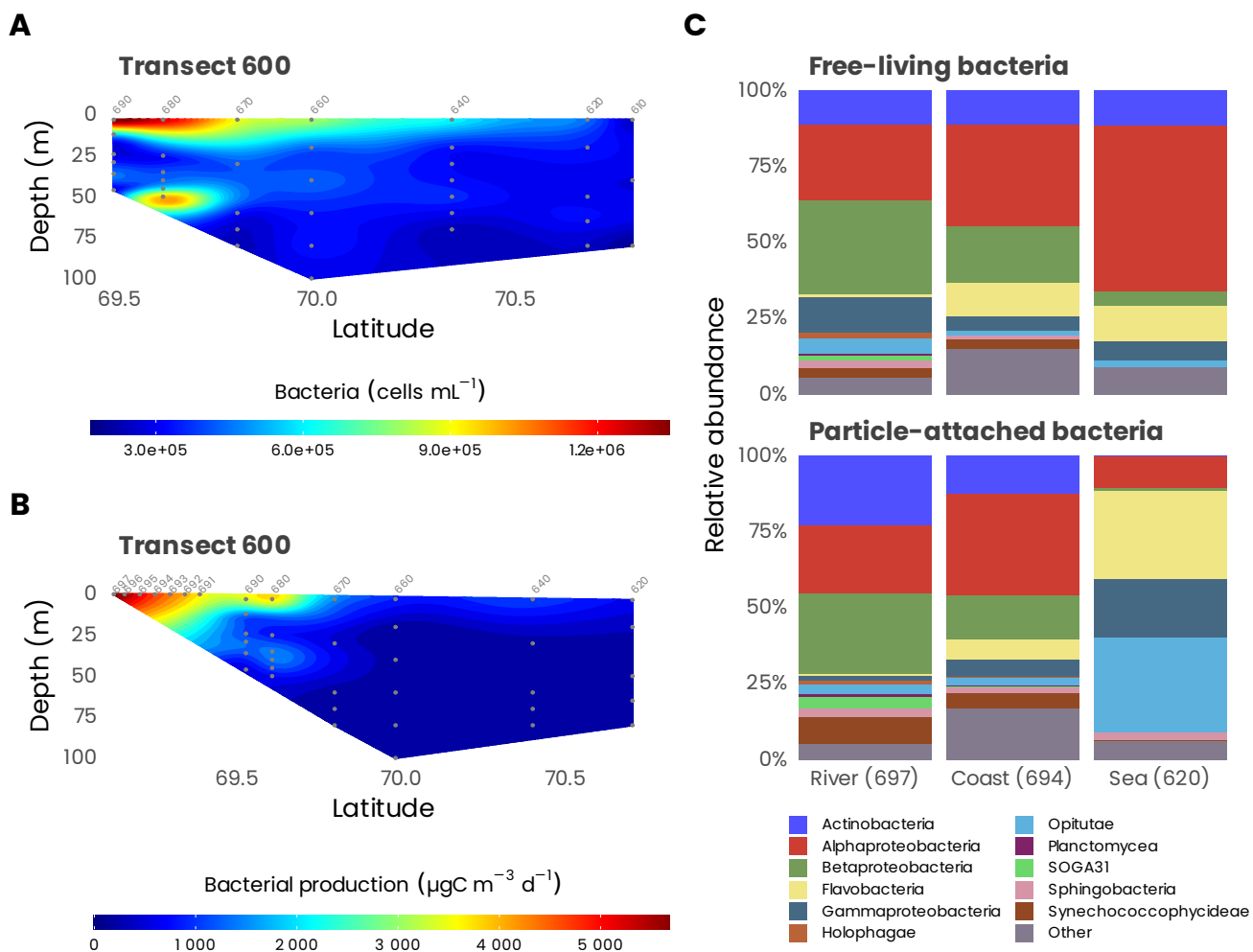
Figure 14. (**A**) Cross-sections of bacterial abundance measured from flow cytometry and (**B**) bacterial production measured along transect 600. Station numbers are identified in light gray on top of each panel. (**C**) Cumulative bar charts comparing the relative class abundances in particle-attached (PA) and free-living (FL) for a selected number of samples in transect 600.

Table 1: Parameters measured during the MALINA oceanographic expedition. Parameters are ordered by alphabetical order.

Parameters	Method	Sampling	Principal investigators
^{137}Cs datation of core samples	Gamma spectrometry	Box corer	Rochon A./ Schmidt
^{137}Cs datation of core samples	Gamma spectrometer	CASQ corer	Rochon A./ Schmidt
^{14}C datation of core samples	Accelerator Mass Spectrometry	Box corer	Rochon A.
^{14}C datation of core samples	Accelerator Mass Spectrometry	CASQ corer	Rochon A.
^{15}N-Ammonium assimilation	^{15}N spiking - incubation - mass-spectrometry	Rosette - Deck incubations	Tremblay J.E./ Raimbault P.
^{15}N-Ammonium assimilation	^{15}N spiking - incubation - mass-spectrometry	Rosette In-situ production line	Tremblay J.E./ Raimbault P.
^{15}N-Ammonium oxidation (Nitrification)	^{15}N spiking - incubation - mass-spectrometry	Rosette - Deck incubations	Tremblay J.E./ Raimbault P.
^{15}N-Ammonium oxidation (Nitrification)	^{15}N spiking - incubation - mass-spectrometry	Rosette In-situ production line	Tremblay J.E./ Raimbault P.
^{15}N-Ammonium primary production (^{13}C)	^{15}N spiking - incubation - mass-spectrometry	Rosette - Deck incubations	Tremblay J.E./ Raimbault P.
^{15}N-Ammonium regeneration	^{15}N spiking - incubation - mass-spectrometry	Rosette - Deck incubations	Tremblay J.E./ Raimbault P.
^{15}N-Ammonium regeneration	^{15}N spiking - incubation - mass-spectrometry	Rosette In-situ production line	Tremblay J.E./ Raimbault P.
^{15}N-N_2 fixation	^{15}N spiking - incubation - mass-spectrometry	Rosette water sample	Tremblay J.E./ Raimbault P.
^{15}N-Nitrate assimilation	^{15}N spiking - incubation - mass-spectrometry	Rosette - Deck incubations	Tremblay J.E./ Raimbault P.
^{15}N-Nitrate assimilation	^{15}N spiking - incubation - mass-spectrometry	Rosette In-situ production line	Tremblay J.E./ Raimbault P.
^{15}N-Urea Photosynthetic parameters	^{15}N incubations mass spectrometry	Rosette Niskin water sample	Tremblay J.E.
^{210}Pb geochronology of core samples	^{209}Po alpha spectrometry	Box corer	Rochon A.
^{210}Pb geochronology of core samples	^{209}Po alpha spectrometry	CASQ corer	Rochon A.
^{226}Ra (particulate)	Gamma spectrometry	Foredeck In-situ pump	Gasser B.
^{226}Ra/^{228}Ra	Gamma spectrometry	Discrete Sample on Continuous System.	Gasser B.
^{234}Th (1 micron < particles > 70 micron)	Beta-counting	Foredeck In-situ pump	Gasser B.
^{234}Th (particles > 70 micron)	Beta-counting	Foredeck In-situ pump	Gasser B.
^{234}Th (Particulate)	Beta-counting	Drifting Sediment trap	Gasser B.
^{234}Th (total)	Beta-counting	Rosette water sample	Gasser B.
^{238}U (Dissolved)	Derived parameter	Rosette water sample	Gasser B.
^{238}U (total)	Alpha-counting	Rosette water sample	Gasser B.
AAPB (abundance)	IR microscopy, fluorimetry. FISH	Rosette water sample	Jeanthon C./ Boeuf D.
AAPB (abundance)	IR microscopy, fluorimetry. FISH	Zodiac water sample	Jeanthon C./ Boeuf D.
Absorption (particulate)	PSICAM	Barge water sample	Leymarie E.
Absorption (particulate)	Spectrophotometer (filters)	Barge water sample	Belanger S.
Absorption (particulate)	Spectrophotometer (filters)	Continuous on way	Belanger S.
Absorption (particulate)	PSICAM	Rosette water sample	Leymarie E.
Absorption (particulate)	Spectrophotometer (filters)	Rosette water sample	Belanger S.
Absorption (particulate)	Spectrophotometer (filters)	Zodiac profiler	Belanger S.
Absorption (total)	PSICAM	Barge water sample	Leymarie E.
Absorption (total)	PSICAM	Rosette water sample	Leymarie E.
Absorption coefficient (total)	HOBI-Labs a-sphere	Barge profiler	Wright V./ Hooker S.
Absorption coefficient (total) (9 wavelengths)	Wetlabs AC9 Serial# 156	Rosette profiler	Ehn J.
Absorption coefficient (total) (9 wavelengths in IR	Wetlabs AC9 Serial# 303	Barge profiler	Doxaran D.
Absorption coefficient (total) (9 wavelengths)	Wetlabs AC9 Serial# 279	Barge profiler	Doxaran D.
Air Relative Humidity	Humidity Sensor	Foredeck Meteorological Tower	Papakyriakou T.
Alkalinity total (TA)	Potentiometry	Barge water sample	Mucci A./ Lansard B.
Alkalinity total (TA)	Potentiometry	Rosette	Mucci A./ Lansard B.
Alkalinity total (TA)	Potentiometry	Zodiac water sample	Mucci A./ Lansard B.
Alkanes	GC-MS	Box corer	Bouloubassi I.
Alkanes	GC-MS	CASQ corer	Bouloubassi I.
Ammonium (NH_4^+) photo-production apparent quantum yield (AQY)	sun simulator - fluorimetry	Rosette water sample	Xie H./ Tremblay J.E.
Ammonium (NH_4^+) photo-production apparent quantum yield (AQY)	sun simulator - fluorimetry	Zodiac water sample	Xie H./ Tremblay J.E.
Aragonite : saturation state	Derived parameter	Barge water sample	Mucci A./ Lansard B.

Table 1: Parameters measured during the MALINA oceanographic expedition. Parameters are ordered by alphabetical order. *(continued)*

Parameters	Method	Sampling	Principal investigators
Aragonite : saturation state	Derived parameter	Rosette water sample	Mucci A./ Lansard B.
Aragonite : saturation state	Derived parameter	Zodiac water sample	Mucci A./ Lansard B.
Archaea (diversity)	CE-SSCP and DNA clone library	Rosette water sample	Joux F.
Attenuation coefficient (total) (9 wavelengths in IR)	Wetlabs AC9 Serial #0303	Barge profiler	Doxaran D.
Attenuation coefficient (total) (9 wavelengths)	Wetlabs AC9 Serial #279	Barge profiler	Doxaran D.
Attenuation coefficient (total) (9 wavelengths)	Wetlabs AC9 Serial #156	Rosette profiler	Ehn J.
Attenuation coefficient at 660 nm	Wetlabs (CRover) transmissometer	Drifting profiling float	Doxaran D.
Backscattering 532 nm	Wetlabs (ECO^3) backscatterometer	Drifting profiling float	Doxaran D.
Backscattering coefficient (3 wavelengths in IR)	Wetlabs ECO-BB3 serial #538	Barge profiler	Doxaran D.
Backscattering coefficient (3 wavelengths)	Wetlabs ECO-BB3 serial #028	Barge profiler	Doxaran D.
Backscattering coefficient (6 Wavelength)	HOBI-Labs Hydroscat-6 serial #	Barge profiler	Wright V./ Hooker S.
Backscattering coefficient (8 wavelengths, spectral)	Hydroscat-6 (ser#97074) and two a-Beta (HOBI-Labs)	Barge profiler	Reynolds R.
Backscattering coefficient (8 wavelengths, spectral)	Hydroscat-6 (ser#97074) and two a-Beta (HOBI-Labs)	Foredeck	Reynolds R.
Backscattering coefficient (9 wavelengths)	Wetlabs ECO-BB9 serial# 274	Rosette profiler	Ehn J.
Bacteria (abundance)	Flow cytometry	Rosette water sample	Vaulot D.
Bacteria (abundance)	Flow Cytometry	Rosette water sample	Joux F./ Ortega E.
Bacterial (abundance)	FISH-TSA	Rosette water sample	Joux F.
Bacterial bio-volume	Epifluorescence microscopy	Rosette water sample	Joux F./ Ortega E.
Bacterial density (benthic)	Flow cytometry	Box corer	Link H./ Archambault P./ Chaillou G.
Bacterial diversity	CE-SSCP and DNA clone library	Rosette water sample	Joux F.
Bacterial Ecto-enzymatic activity	Spectrofluorimetry	Rosette water sample	Joux F./ Ortega E.
Bacterial growth (limitation by nutrients)	Leucine-^{3}H incubations - cells counts	Rosette water sample	Joux F./ Jeffrey W./ Ortega E.
Bacterial production	Leucine-^{3}H incorporation	Rosette water sample	Joux F./ Jeffrey W.
Bacterial production	Leucine-^{3}H incorporation	Zodiac water sample	Joux F./ Jeffrey W.
Bacterial production (effects of DOM UV exposure on...)	Leucine-^{3}H incorporation - cell counts	Rosette water sample	Joux F./ Jeffrey W./ Ortega E.
Bacterial production (effects of UV radiation)	Leucine-^{3}H incorporation	Rosette water sample	Joux F./ Jeffrey W.
Bacterial respiration (whole community)	O^2 consumption - Winkler - Incubations	Rosette water sample	Joux F./ Ortega E.
Benthic ammonium flux	Incubations - Colorimetry	Box corer	Link H./ Archambault P./ Chaillou G.
Benthic DOC remineralisation	Incubations - wet oxidation	Box corer	Link H./ Archambault P./ Chaillou G./ Charriere B.
Benthic Macrofauna abundance	Microscopy	Box corer	Link H./ Archambault P./ Chaillou G.
Benthic Macrofauna biomass	Wet weight	Box corer	Link H./ Archambault P./ Chaillou G.
Benthic Macrofauna diversity	Microscopy	Box corer	Link H./ Archambault P./ Chaillou G.
Benthic nitrate flux	Incubations - Colorimetry- Autoanalyzer	Box corer	Link H./ Archambault P./ Chaillou G.
Benthic nitrite flux	Incubations - Colorimetry- Autoanalyzer	Box corer	Link H./ Archambault P./ Chaillou G.
Benthic phosphate flux	Incubations - Colorimetry- Autoanalyzer	Box corer	Link H./ Archambault P./ Chaillou G.
Benthic respiration	Incubations - Optic - Oxygen probe	Box corer	Link H./ Archambault P./ Chaillou G.
Benthic silicic acid flux	Incubations - Colorimetry - Autoanalyzer	Box corer	Link H./ Archambault P./ Chaillou G.
Bioturbation of sediments	Incubation with luminophores	Box corer	Link H./ Archambault P./ Chaillou G.
Calcite : saturation state	Derived parameter	Barge water sample	Mucci A./ Lansard B.
Calcite : saturation state	derived parameter	Rosette water sample	Mucci A./ Lansard B.
Calcite : saturation state	Derived parameter	Zodiac water sample	Mucci A./ Lansard B.
Campesterol, cholesterol, sistosterol and products of degrad	GC-MS	Rosette water sample	Sempere R.
CDOM absorption	PSICAM	Barge water sample	Leymarie E.
CDOM absorption	Spectrophotometer	Barge water sample	Matsuoka A./ Bricaud A.
CDOM absorption	Spectrophotometer	Barge water sample	Wright V./ Hooker S.
CDOM absorption	Ultrapath	Barge water sample	Bricaud A.
CDOM absorption	PSICAM	Rosette water sample	Leymarie E.
CDOM absorption	Spectrophotometer	Rosette water sample	Matsuoka A./ Bricaud A.

Table 1: Parameters measured during the MALINA oceanographic expedition. Parameters are ordered by alphabetical order. *(continued)*

Parameters	Method	Sampling	Principal investigators
CDOM absorption	Ultrapath	Rosette water sample	Bricaud A.
CDOM absorption	PSICAM	Zodiac water sample	Leymarie E.
CDOM absorption	Spectrophotometer	Zodiac water sample	Matsuoka A./ Bricaud A.
CDOM absorption	Ultrapath	Zodiac water sample	Bricaud A.
CDOM fluorescence	HOBI-Labs Hydroscat-6 ser# HS080542	Barge profiler	Wright V./ Hooker S.
CDOM fluorescence	Wetlabs WetStar WSCD	Barge profiler	Doxaran D.
CDOM fluorescence	Wetlabs (ECO^3) fluorometer	Drifting profiling float	Doxaran D.
CDOM fluorescence	Haardt fluorometer	Rosette profiler	Belanger S./ Amon/ Sempere R.
CDOM fluorescence EEM (excitation-emission-matrix)	Spectrofluorimetry	Rosette water sample	Belanger S./ Amon/ Sempere R.
CDOM fluorescence EEM (excitation-emission-matrix)	Spectrofluorimetry	Zodiac water sample	Belanger S./ Amon/ Sempere R.
Chlorophyll a and Phaeopigments (concentration)	Fluorimetry Size fractionned	Rosette water sample	Gosselin M./ Belanger S.
Chlorophyll a and Phaeopigments (benthic)	Fluorometric analysis	Box corer	Link H./ Archambault P./ Chaillou G.
Chlorophyll a fluorescence [Fchla (z)]	Chelsea Mini-Track a II fluorometer	Barge profiler	Doxaran D.
Chlorophyll a fluorescence [Fchla (z)]	HOBI-Labs Hydroscat-6 fluorometer	Barge profiler	Wright V./ Hooker S.
Chlorophyll a fluorescence [Fchla (z)]	Wetlabs (ECO^3) fluorometer	Drifting profiling float	Doxaran D.
Chlorophyll a fluorescence [Fchla (z)]	SeaPoint fluorometer	Rosette profiler	Gratton Y./ Prieur L./ Tremblay J.E.
CO photo-prod. apparent quantum yield for CDOM	Sun simulator - reduction gas analyzer	Rosette water sample	Xie H.
CO photo-prod. apparent quantum yield for CDOM	Sun simulator - reduction gas analyzer	Zodiac water sample	Xie H.
CO photo-prod. apparent quantum yield for particulate matter	Sun simulator - reduction gas analyzer	Rosette water sample	Xie H.
CO photo-prod. apparent quantum yield for particulate matter	Sun simulator - reduction gas analyzer	Zodiac water sample	Xie H.
CO^2 (atm) concentration	Infra Red	Foredeck Meteorological Tower	Papakyriakou T.
CO^2 (seawater) concentration	Infra Red	Foredeck Meteorological Tower	Papakyriakou T.
CO^3 2- concentrations	Derived parameter	Barge water sample	Mucci A./ Lansard B.
CO^3 2- concentrations	Derived parameter	Rosette water sample	Mucci A./ Lansard B.
CO^3 2- concentrations	Derived parameter	Zodiac water sample	Mucci A./ Lansard B.
Coccolithophorids	Microscopy	Rosette water sample	Coupel P.
Conductivity (z)	Sensor on SBE Fascat CTD serial #	Barge profiler	Doxaran D.
Conductivity (z)	Sensor on SBE Fascat CTD serial #	Barge profiler	Wright V./ Hooker S.
Conductivity (z)	Sensor SeaBird 4c on CTD SBE-911	Rosette profiler	Gratton Y./ Prieur L.
CTD	Seabird	Drifting profiling float	Doxaran D.
Cultures of sorted populations	Sorted by flow cytometry, serial dilution and single cell pipetting	Rosette water sample	Vaulot D.
Current Profile [U (z)]	ADCP (LADCP) RD Instrument 300 KHz	Rosette profiler	Marec C./ Gratton Y./ Prieur L.
delta ^{13}C	Mass Spectrometry	Zodiac water sample	Mucci A./ Lansard B.
delta ^{13}C on suspended particulate matter	Mass Spectrometry	Rosette water sample	Tremblay J.E./ Raimbault P.
delta ^{15}C on suspended particulate matter	Mass Spectrometry	Rosette water sample	Tremblay J.E./ Raimbault P.
delta ^{18}O - water	Mass Spectrometry	Rosette water sample	Mucci A./ Lansard B.
delta ^{18}O - water	Mass Spectrometry	Zodiac water sample	Mucci A./ Lansard B.
delta^{13}C	Mass Spectrometer	Barge water sample	Mucci A./ Lansard B.
delta^{13}C	Mass Spectrometry	Rosette water sample	Mucci A./ Lansard B.
delta^{18}O - water	Mass Spectrometry	Barge water sample	Mucci A./ Lansard B.
Diacids composition	GC/MS	Rosette water sample	Sempere R.
Diacids composition	GC/MS	Zodiac water sample	Sempere R.
Diacids photo-production apparent quantum yield (AQY)	Sun simulator - GC/MS	Zodiac water sample	Sempere R.
Dinoflagellates cysts Abundance	Microscopy	Box corer	Rochon A.
Dinoflagellates cysts Abundance	Microscopy	CASQ corer	Rochon A.
Dinoflagellates cysts Identification	Microscopy	Box corer	Rochon A.
Dinoflagellates cysts Identification	Microscopy	CASQ corer	Rochon A.
Dissolved Inorg. Carbon photo-prod. apparent quantum yield	Sun simulator - indrared CO^2 analyzer	Rosette water sample	Xie H./ Belanger S.
Dissolved Inorg. Carbon photo-prod. apparent quantum yield	Sun simulator - indrared CO^2 analyzer	Zodiac water sample	Xie H./ Belanger S.

Table 1: Parameters measured during the MALINA oceanographic expedition. Parameters are ordered by alphabetical order. *(continued)*

Parameters	Method	Sampling	Principal investigators
Dissolved Organic Carbon (DOC)	High Temperature Catalytic Oxidation	Barge water sample	Wright V./ Hooker S.
Dissolved Organic Carbon (DOC)	High Temperature Catalytic Oxidation	Rosette water sample	Sempere R.
Dissolved Organic Carbon (DOC)	High Temperature Catalytic Oxidation	Rosette water sample	Benner R.
Dissolved Organic Carbon (DOC)	Wet oxidation	Rosette water sample	Tremblay J.E./ Raimbault P.
Dissolved Organic Carbon (DOC)	High Temperature Catalytic Oxidation	Zodiac water sample	Sempere R.
Dissolved Organic Carbon (DOC)	High Temperature Catalytic Oxidation	Zodiac water sample	Benner R.
Dissolved Organic Nitrogen (DON)	Wet oxidation	Rosette water sample	Tremblay J.E./ Raimbault P.
Dissolved Organic Nitrogen (Total) (TDON)	High Temperature Catalytic Oxidation	Rosette water sample	Benner R.
Dissolved Organic Nitrogen (Total) (TDON)	High Temperature Catalytic Oxidation	Zodiac water sample	Benner R.
Dissolved Organic Phosphorus (DOP)	Wet oxidation	Rosette water sample	Tremblay J.E./ Raimbault P.
Ed, Lu, Eu, Es	C-OPS package (320, 340, 380, 395 nm)	Barge profiler	Hooker
Electric resistivity (sediment core physical properties)	Geotek Multi Sensor Core Logger	Box corer	Rochon A.
Electric resistivity (sediment core physical properties)	Geotek Multi Sensor Core Logger	CASQ corer	Rochon A.
Eukaryotes (abundance)	DAPI epifluorescence microscopy	Rosette water sample	Lovejoy C.
Eukaryotes (abundance)	FISH-TSA	Rosette water sample	Lovejoy C.
Eukaryotes (biomass)	DAPI epifluorescence microscopy	Rosette water sample	Lovejoy C.
fCO_2	Derived parameter	Barge water sample	Mucci A./ Lansard B.
fCO_2	Derived parameter	Rosette water sample	Mucci A./ Lansard B.
fCO_2	Derived parameter	Zodiac water sample	Mucci A./ Lansard B.
Foraminifera abundance	Microscopy	Box corer	Rochon A.
Foraminifera abundance	Microscopy	CASQ corer	Rochon A.
Foraminifera identification	Microscopy	Box corer	Rochon A.
Foraminifera identification	Microscopy	CASQ corer	Rochon A.
Gamma density (sediment core physical properties)	Geotek Multi Sensor Core Logger	Box corer	Rochon A.
Gamma density (sediment core physical properties)	Geotek Multi Sensor Core Logger	CASQ corer	Rochon A.
H_2O (atm) concentration	Infrared gas analyzer	Foredeck Meteorological Tower	Papakyriakou T.
HCO_2^- concentration	Derived parameter	Barge water sample	Mucci A./ Lansard B.
HCO_2^- concentration	Derived parameter	Rosette water sample	Mucci A./ Lansard B.
HCO_2^- concentration	Derived parameter	Zodiac water sample	Mucci A./ Lansard B.
Hydro SCAMP (Temp, Salin, Chlorophyll, turb. ...)	SCAMP profiler	In-water profiler	Gratton Y.
Hydrolysable Amino Acids (Total) (THAA)	HPLC	Rosette water sample	Benner R.
Hydrolysable Amino Acids (Total) (THAA)	HPLC	Zodiac water sample	Benner R.
Hydroxyl radicals (OH)	HPLC	Rosette water sample	Sempere R.
Hydroxyl radicals (OH)	HPLC	Zodiac water sample	Sempere R.
Hydroxyl radicals (OH) photo-prod. apparent quantum yield	Sun simulator - HPLC	Rosette water sample	Sempere R.
Hydroxyl radicals (OH) photo-prod. apparent quantum yield	Sun simulator - HPLC	Zodiac water sample	Sempere R.
IP25 (C25 Monounsaturated Hydrocarbon)	GC	Box corer	Masse G.
IP25 (C25 Monounsaturated Hydrocarbon)	GC	CASQ corer	Masse G.
Irradiance	Satlantic (PUV) (305,325, 340, 380,..)	Foredeck	Sempere R.
Irradiance (412, 490, 555 nm)	Satlantic (OCR) radiometer	Drifting profiling float	Doxaran D.
Lignin phenols (dissolved)	GC/MS	Rosette water sample	Benner R.
Lignin phenols (dissolved)	GC/MS	Zodiac water sample	Benner R.
Lipid biomarqueurs	GC-Flamme Ionization Detection / GC-MS	Box corer	Tolosa I.
Lipid biomarqueurs	GC-Flamme Ionization Detection / GC-MS	CASQ corer	Tolosa I.
Lipid biomarqueurs $d^{13}C$	GC-Combustion Isotope ratio MS	Box corer	Tolosa I.
Lipid biomarqueurs $d^{13}C$	GC-Combustion Isotope ratio MS	CASQ corer	Tolosa I.
Long-Wave radiation (Lwin)	Pyrgeometer	Wheel-house radiation platform	Papakyriakou T.
Magnetic susceptibility (sediment core physical properties)	Geotek Multi Sensor Core Logger	Box corer	Rochon A.

Table 1: Parameters measured during the MALINA oceanographic expedition. Parameters are ordered by alphabetical order. *(continued)*

Parameters	Method	Sampling	Principal investigators
Magnetic susceptibility (sediment core physical properties)	Geotek Multi Sensor Core Logger	CASQ corer	Rochon A.
Nanoeukaryotes (abundance)	Flow cytometry	Rosette water sample	Vaulot D.
NH_4^+	Fluorescence	Rosette water sample	Tremblay J.E./ Raimbault P.
Nitrate (concentration)	Satlantic ISUS	Rosette profiler	Gratton Y./ Prieur L./ Tremblay J.E.
NO_2^-	Colorimetry/Autoanalyzer	Rosette water sample	Tremblay J.E./ Raimbault P.
NO_3^-	Colorimetry/Autoanalyzer	Rosette water sample	Tremblay J.E./ Raimbault P.
Organic Compounds High Molecular Weight (HMW)	Sun simulator incubations - HPLC	Rosette water sample	Xie H.
Organic Compounds High Molecular Weight (HMW)	Sun simulator incubations - HPLC	Zodiac water sample	Xie H.
Organic Compounds Low Molecular Weight (LMW)	Sun simulator incubations - HPLC	Rosette water sample	Xie H.
Organic Compounds Low Molecular Weight (LMW)	Sun simulator incubations - HPLC	Zodiac water sample	Xie H.
Oxygen (dissolved)	Discrete samples Winkler Method	Barge water sample	Prieur L.
Oxygen (dissolved)	Idronaut Ocean Seven O^2 sensor	Continuous horizontal	Papakyriakou T.
Oxygen (dissolved)	SeaBird SBE-43 sensor	Rosette profiler	Gratton Y./ Prieur L.
Oxygen (dissolved)	Discrete samples Winkler Method	Rosette water sample	Prieur L.
Oxygen (dissolved)	Discrete samples Winkler Method	Zodiac water sample	Prieur L.
P-waves speed (sediment core physical properties)	Geotek Multi Sensor Core Logger	Box corer	Rochon A.
P-waves speed (sediment core physical properties)	Geotek Multi Sensor Core Logger	CASQ corer	Rochon A.
Paleomagnetism	Cryogenic magnetometer	Box corer	Rochon A.
Paleomagnetism	Cryogenic magnetometer	CASQ corer	Rochon A.
PAR	Biospherical sensor	Barge profiler	Wright V./ Hooker S.
PAR	Biospherical sensor	Rosette profiler	Gratton Y./ Prieur L./ Tremblay J.E.
PAR	PARLite sensor	Wheel-house radiation platform	Papakyriakou T.
Particle Size Distribution	LISST-100X	Barge profiler	Reynolds R.
Particle Size Distribution	Coulter counter	Barge water sample	Reynolds R.
Particle Size Distribution	UVP-5	In-water profiler	Picheral M.
Particle Size Distribution	LISST-100X	Rosette profiler	Reynolds R.
Particle Size Distribution	Coulter counter	Rosette water sample	Reynolds R.
Particulate Organic Carbon (POC)	CHN analyzer	Barge water sample	Wright V./ Hooker S.
Particulate Organic Carbon (POC)	CHN analyzer on SPM filters	Barge water sample	Doxaran D./ Ehn J./ Babin M.
Particulate Organic Carbon (POC)	CHN analyzer on SPM filters	Rosette water sample	Doxaran D./ Ehn J./ Babin M.
Particulate Organic Carbon (POC)	Wet oxidation	Rosette water sample	Tremblay J.E./ Raimbault P.
Particulate Organic Carbon (POC)	CHN analyzer on SPM filters	Zodiac water sample	Doxaran D./ Ehn J./ Babin M.
Particulate Organic Matter (POM)	CHN analyzer on SPM filters	Barge water sample	Wright V./ Hooker S.
Particulate Organic Nitrogen (PON)	CHN analyzer	Barge water sample	Wright V./ Hooker S.
Particulate Organic Nitrogen (PON)	Wet oxidation	Rosette water sample	Tremblay J.E./ Raimbault P.
Particulate Organic Phosphorus (POP)	Wet oxidation	Rosette water sample	Tremblay J.E./ Raimbault P.
pH	Spectrophotometry	Barge water sample	Mucci A./ Lansard B.
pH	SeaBird SBE-18 sensor	Rosette profiler	Gratton Y./ Prieur L./ Tremblay J.E.
pH	Spectrophotometry	Rosette water sample	Mucci A./ Lansard B.
pH	Spectrophotometry	Zodiac water sample	Mucci A./ Lansard B.
pH (total proton scale)	Derived parameter	Barge water sample	Mucci A./ Lansard B.
pH (total proton scale)	Dervide parameter	Rosette water sample	Mucci A./ Lansard B.
pH (total proton scale)	Dervide parameter	Zodiac water sample	Mucci A./ Lansard B.
Photosynthetic eukaryotes (morphology)	Scanning Electron Microscopy	Rosette water sample	Vaulot D.
Photosynthetic eukaryotes (diversity)	DNA clone library and TRFLP of sorted populations	Rosette water sample	Vaulot D.
Photoheterotrophs (diel cycle genes analyses)	RNA expression every 4 hours	Rosette water sample	Jeanthon C./ Boeuf D.
Photoheterotrophs (DNA diversity)	DNA clone library	Rosette water sample	Jeanthon C./ Boeuf D.
Photoheterotrophs (metagenome)	454 sequencing	Rosette water sample	Jeanthon C./ Boeuf D.

Table 1: Parameters measured during the MALINA oceanographic expedition. Parameters are ordered by alphabetical order. *(continued)*

Parameters	Method	Sampling	Principal investigators
Photosynthetic parameters	^{14}C incubations	Rosette water sample	Huot Y.
Phytoplankton (abundance)	Inverted microscope	Rosette water sample	Gosselin M./ Belanger S.
Phytoplankton (taxonomy)	Inverted microscope	Rosette water sample	Gosselin M./ Belanger S.
Phytoplankton pigments	HPLC	Barge water sample	Wright V./ Hooker S.
Phytoplankton pigments	HPLC	Rosette water sample	Ras J./ Claustre H.
Picoeukaryotes (abundance)	Flow cytometry	Rosette water sample	Vaulot D.
Picoplankton (diversity)	DNA clone library	Rosette water sample	Lovejoy C.
Photosynthetic eukaryotes (diversity)	DNA from filters	Rosette water sample	Vaulot D.
Picoplankton (diversity)	RNA clone library	Rosette water sample	Lovejoy C.
Plankton taxonomy	UVP-5	In-water profiler	Picheral M./ Marec C.
$(PO_4)^{3-}$	Colorimetry/Autoanalyzer	Rosette water sample	Tremblay J.E./ Raimbault P.
Pollen and Spores Abundance	Microscopy	Box corer	Rochon A.
Pollen and Spores Abundance	Microscopy	CASQ corer	Rochon A.
Pollen and Spores Identification	Microscopy	Box corer	Rochon A.
Pollen and Spores Identification	Microscopy	CASQ corer	Rochon A.
PR-containing bacteria (abundance)	Q-PCR	Rosette water sample	Jeanthon C./ Boeuf D.
Pressure (Barometric)	Pressure Sensor	Foredeck Meteorological Tower	Papakyriakou T.
Radiance	Camera Luminance	Profile mode	Antoine D./ Leymarie E.
Radiance	Camera Luminance	Surface mode	Antoine D./ Leymarie E.
Radiance (surface leaving radiance)	BIO-SHADE	Barge profiler	Hooker
Radiance (surface leaving radiance)	BIOSORS	Foredeck	Hooker
Radiance (surface leaving radiance)	Satlantic HyperSAS	Foredeck	Belanger S.
Radiance (surface leaving radiance)	TriOS above water sensor	Foredeck	Doxaran D.
Radiance : Sub Product : average cosines	Camera Luminence	Profile mode	Antoine D./ Leymarie E.
Radiance : Sub Product : average cosines	Camera Luminence	Surface mode	Antoine D./ Leymarie E.
Radiance : Sub Product : irradiance (E)	Camera Luminence	Profile mode	Antoine D./ Leymarie E.
Radiance : Sub Product : irradiance (E)	Camera Luminence	Surface mode	Antoine D./ Leymarie E.
Radiance : Sub Product : Lnadir	Camera Luminence	Profile mode	Antoine D./ Leymarie E.
Radiance : Sub Product : Lnadir	Camera Luminence	Surface mode	Antoine D./ Leymarie E.
Radiance : Sub Product : Qnadir	Camera Luminence	Profile mode	Antoine D./ Leymarie E.
Radiance : Sub Product : Qnadir	Camera Luminence	Surface mode	Antoine D./ Leymarie E.
Radiance : Sub Product : scalar irradiance (Escal)	Camera Luminence	Profile mode	Antoine D./ Leymarie E.
Radiance : Sub Product : scalar irradiance (Escal)	Camera Luminence	Surface mode	Antoine D./ Leymarie E.
Rotational movement (accx, accy, accz,rx,ry,rz)	multi-axis inertial sensing system	Foredeck Meteorological Tower	Papakyriakou T.
Salinity	Salinometer	Barge water sample	Gratton Y./ Prieur L.
Salinity	Salinometer	Rosette water sample	Gratton Y./ Prieur L.
Salinity (sea surface) SSS	Thermosalinograph - underway system	Continuous horizontal	Papakyriakou T.
Salinity [S (z)]	Derived parameter from SBE Fastcat LOC IOP pack.	Barge profiler	Doxaran D.
Salinity [S (z)]	Derived parameter from SBE Fastcat NASA IOP pack.	Barge profiler	Wright V./ Hooker S.
Salinity [S (z)]	Derived parameter	Rosette profiler	Gratton Y./ Prieur L./ Tremblay J.E.
Short-Wave radiation (Swin)	Pyranometer	Wheel-house radiation platform	Papakyriakou T.
Si (OH)$_4$	Colorimetry/Autoanalyzer	Rosette water sample	Tremblay J.E./ Raimbault P.
SPM (Suspended Particulate Material)	dry weight (gravimetry)	Barge water sample	Wright V./ Hooker S.
SPM (Suspended Particulate Material)	dry weight (gravimetry)	Barge water sample	Doxaran D./ Ehn J./ Babin M.
SPM (Suspended Particulate Material)	dry weight (gravimetry)	Rosette water sample	Doxaran D./ Ehn J./ Babin M.
SPM (Suspended Particulate Material)	dry weight (gravimetry)	Zodiac water sample	Doxaran D./ Ehn J./ Babin M.
Sugars	HPLC	Rosette water sample	Sempere R.
Sugars	HPLC	Zodiac water sample	Sempere R.
Synechococcus (abundance)	Flow cytometry	Rosette water sample	Vaulot D.

Table 1: Parameters measured during the MALINA oceanographic expedition. Parameters are ordered by alphabetical order. *(continued)*

Parameters	Method	Sampling	Principal investigators
Temperature (Air)	Temperature Sensor	Foredeck Meteorological Tower	Papakyriakou T.
Temperature (Sea Surface)	Thermosalinograph - underway system	Continuous horizontal	Papakyriakou T.
Temperature (Surface Skin)	IR transducer	Foredeck Meteorological Tower	Papakyriakou T.
Temperature [T (z)]	Temp sensor on SBE Fastcat CTD serial #	Barge profiler	Doxaran D.
Temperature [T (z)]	Temp sensor on SBE Fastcat CTD serial #	Barge profiler	Wright V./ Hooker S.
Temperature [T (z)]	Sensor SeaBird 3plus on CTD SBE-911	Rosette profiler	Gratton Y./ Prieur L./ Tremblay J.E.
Total Inorganic Carbon (TIC)	Derived parameter	Barge water sample	Mucci A./ Lansard B.
Total Inorganic Carbon (TIC)	Derived parameter	Rosette water sample	Mucci A./ Lansard B.
Total Inorganic Carbon (TIC)	Derived parameter	Zodiac water sample	Mucci A./ Lansard B.
Total Organic Carbon (TOC)	Wet oxidation	Rosette water sample	Tremblay J.E./ Raimbault P.
Total Organic Nitrogen (TON)	Wet oxidation	Rosette water sample	Tremblay J.E./ Raimbault P.
Total Organic Phosphorus (TOP)	Wet oxidation	Rosette water sample	Tremblay J.E./ Raimbault P.
Trace metals	X-Ray fluorescence spectroscopy	Box corer	Martinez P.
Trace metals	X-Ray fluorescence spectroscopy	CASQ corer	Martinez P.
Urea (concentration)	Spectrophotometry	Rosette water sample	Tremblay J.E./ Raimbault P.
Volume Scattering Function (VSF)	Benchtop use of POLVSM	Barge water sample	Chami M.
Volume Scattering Function (VSF)	Benchtop use of POLVSM	Rosette water sample	Chami M.
Volume Scattering Function (VSF)	Benchtop use of POLVSM	Zodiac water sample	Chami M.
Wind direction	Vane	Foredeck Meteorological Tower	Papakyriakou T.
Wind speed	Anemometer	Foredeck Meteorological Tower	Papakyriakou T.
Major and minor elements	XRF core scanner	CASQ corer	Martinez P.

Author contributions. See Table 1 for the complete list of measured variables with their associated PIs.

Competing interests. The authors declare no competing interests.

430 *Acknowledgements.* This work is dedicated to the memory of Captain Marc Thibault (commanding officer of the *CCGS Amundsen,* Canadian Coast Guard), Daniel Dubé (*CCGS Amundsen* helicopter pilot, Transport Canada) and Dr. Klaus Hochheim (research scientist at the Centre for Earth Observation Science, University of Manitoba) who died in the *CCGS Amundsen* helicopter crash on the evening of 2013-09-09 in the icy waters of McClure Strait in the Canadian Arctic. We are very grateful to the captain (Marc Thibault) and crews of the Canadian research icebreaker *CCGS Amundsen* during the Malina cruise in the Beaufort Sea. This study

435 was conducted as part of the Malina scientific program funded by ANR (Agence Nationale de la Recherche), INSU-CNRS (Institut National des Sciences de l'Univers - Centre National de la Recherche Scientifique), CNES (Centre National d'Études Spatiales) and ESA (European Space Agency). The International Atomic Energy Agency is grateful to the Government of the Principality of Monaco for the support provided to its Environment Laboratories.

References

440   Abdul Aziz, O. I. and Burn, D. H.: Trends and variability in the hydrological regime of the Mackenzie River Basin, Journal of Hydrology, 319, 282–294, https://doi.org/10.1016/j.jhydrol.2005.06.039, https://linkinghub.elsevier.com/retrieve/pii/S0022169405003665, 2006.

Aminot, A. and Kérouel, R.: Dosage automatique des nutriments dans les eaux marines : méthodes en flux continu., Ifremer (April 1 2007), 2007.

445   Amon, R. R., Budéus, G., and Meon, B.: Dissolved organic carbon distribution and origin in the Nordic Seas: Exchanges with the Arctic Oean and the North Atlantic, Journal of Geophysical Research, 108, 14–1, https://doi.org/10.1029/2002jc001594, http://doi.wiley.com/10.1029/2002JC001594, 2003.

Antoine, D., Hooker, S. B., Bélanger, S., Matsuoka, A., and Babin, M.: Apparent optical properties of the Canadian Beaufort Sea – Part 1: Observational overview and water column relationships, Biogeosciences, 10, 4493–4509, https://doi.org/10.5194/bg-10-4493-2013, https://www.biogeosciences.net/10/4493/2013/https://bg.copernicus.org/articles/10/4493/2013/, 2013.

450

Ardyna, M., Babin, M., Devred, E., Forest, A., Gosselin, M., Raimbault, P., and Tremblay, J.-É.: Shelf-basin gradients shape ecological phytoplankton niches and community composition in the coastal Arctic Ocean (Beaufort Sea), Limnology and Oceanography, 62, 2113–2132, https://doi.org/10.1002/lno.10554, http://doi.wiley.com/10.1002/lno.10554, 2017.

Asmala, E., Autio, R., Kaartokallio, H., Pitkänen, L., Stedmon, C. A., and Thomas, D. N.: Bioavailability of riverine dissolved
455   organic matter in three Baltic Sea estuaries and the effect of catchment land use, Biogeosciences, 10, 6969–6986, https://doi.org/10.5194/bg-10-6969-2013, http://www.biogeosciences.net/10/6969/2013/, 2013.

Balzano, S., Gourvil, P., Siano, R., Chanoine, M., Marie, D., Lessard, S., Sarno, D., and Vaulot, D.: Diversity of cultured photosynthetic flagellates in the northeast Pacific and Arctic Oceans in summer, Biogeosciences, 9, 4553–4571, https://doi.org/10.5194/bg-9-4553-2012, https://www.biogeosciences.net/9/4553/2012/, 2012.

460   Balzano, S., Percopo, I., Siano, R., Gourvil, P., Chanoine, M., Marie, D., Vaulot, D., and Sarno, D.: Morphological and genetic diversity of Beaufort Sea diatoms with high contributions from the Chaetoceros neogracilis species complex, Journal of Phycology, 53, 161–187, https://doi.org/10.1111/jpy.12489, http://doi.wiley.com/10.1111/jpy.12489, 2017.

Bélanger, S., Xie, H. X., Krotkov, N., Larouche, P., Vincent, W. F., and Babin, M.: Photomineralization of terrigenous dissolved organic matter in Arctic coastal waters from 1979 to 2003: Interannual variability and implications of climate change, Global
465   Biogeochemical Cycles, 20, 2006.

Bélanger, S., Cizmeli, S. A., Ehn, J., Matsuoka, A., Doxaran, D., Hooker, S., and Babin, M.: Light absorption and partitioning in Arctic Ocean surface waters: impact of multiyear ice melting, Biogeosciences, 10, 6433–6452, https://doi.org/10.5194/bg-10-6433-2013, www.biogeosciences.net/10/6433/2013/https://www.biogeosciences.net/10/6433/2013/http://www.biogeosciences.net/10/6433/2013/, 2013.

470   Benner, R. and Strom, M.: A critical evaluation of the analytical blank associated with DOC measurements by high-temperature catalytic oxidation, Marine Chemistry, 41, 153–160, https://doi.org/10.1016/0304-4203(93)90113-3, https://linkinghub.elsevier.com/retrieve/pii/0304420393901133, 1993.

Berggren, M., Laudon, H., and Jansson, M.: Aging of allochthonous organic carbon regulates bacterial production in unproductive boreal lakes, Limnology and Oceanography, 54, 1333–1342, https://doi.org/10.4319/lo.2009.54.4.1333, http://doi.wiley.com/
475   10.4319/lo.2009.54.4.1333, 2009.

Carmack, E. C. and Macdonald, R. W.: Oceanography of the Canadian Shelf of the Beaufort Sea: A Setting for Marine Life, ARCTIC, 55, https://doi.org/10.14430/arctic733, https://journalhosting.ucalgary.ca/index.php/arctic/article/view/63790, 2002.

Carmack, E. C., Macdonald, R. W., and Papadakis, J. E.: Water mass structure and boundaries in the Mackenzie shelf estuary, Journal of Geophysical Research, 94, 18 043, https://doi.org/10.1029/JC094iC12p18043, http://doi.wiley.com/10.1029/JC094iC12p18043, 1989.

Commission of the European Community: Manual of quality control procedures for validation of oceanographic data., p. 436, 1993.

Coupel, P., Matsuoka, A., Ruiz-Pino, D., Gosselin, M., Marie, D., Tremblay, J.-É., and Babin, M.: Pigment signatures of phytoplankton communities in the Beaufort Sea, Biogeosciences, 12, 991–1006, https://doi.org/10.5194/bg-12-991-2015, www.biogeosciences.net/12/991/2015/https://www.biogeosciences.net/12/991/2015/, 2015.

Doxaran, D., Ehn, J., Bélanger, S., Matsuoka, A., Hooker, S., and Babin, M.: Optical characterisation of suspended particles in the Mackenzie River plume (Canadian Arctic Ocean) and implications for ocean colour remote sensing, Biogeosciences, 9, 3213–3229, https://doi.org/10.5194/bg-9-3213-2012, https://www.biogeosciences.net/9/3213/2012/, 2012.

Doxaran, D., Devred, E., and Babin, M.: A 50 terrestrial particles delivered by the Mackenzie River into the Beaufort Sea (Canadian Arctic Ocean) over the last 10 years, Biogeosciences, 12, 3551–3565, https://doi.org/10.5194/bg-12-3551-2015, www.biogeosciences.net/12/3551/2015/, 2015.

Ehn, J. K., Reynolds, R. A., Stramski, D., Doxaran, D., Lansard, B., and Babin, M.: Patterns of suspended particulate matter across the continental margin in the Canadian Beaufort Sea during summer, Biogeosciences, 16, 1583–1605, https://doi.org/10.5194/bg-16-1583-2019, https://www.biogeosciences.net/16/1583/2019/, 2019.

Fichot, C. G. and Benner, R.: A novel method to estimate DOC concentrations from CDOM absorption coefficients in coastal waters, Geophysical Research Letters, 38, https://doi.org/10.1029/2010GL046152, http://doi.wiley.com/10.1029/2010GL046152, 2011.

Fichot, C. G. and Miller, W. L.: An approach to quantify depth-resolved marine photochemical fluxes using remote sensing: Application to carbon monoxide (CO) photoproduction, Remote Sensing of Environment, 114, 1363–1377, https://doi.org/10.1016/j.rse.2010.01.019, http://linkinghub.elsevier.com/retrieve/pii/S0034425710000507, 2010.

Fichot, C. G., Kaiser, K., Hooker, S. B., Amon, R. M. W., Babin, M., Bélanger, S., Walker, S. A., and Benner, R.: Pan-Arctic distributions of continental runoff in the Arctic Ocean, Scientific Reports, 3, 1053, https://doi.org/10.1038/srep01053, http://www.nature.com/articles/srep01053http://www.pubmedcentral.nih.gov/articlerender.fcgi?artid=3542531&tool=pmcentrez&rendertype=abstract, 2013.

Fichot, C. G., Benner, R., Kaiser, K., Shen, Y., Amon, R. M. W., Ogawa, H., and Lu, C.-J.: Predicting Dissolved Lignin Phenol Concentrations in the Coastal Ocean from Chromophoric Dissolved Organic Matter (CDOM) Absorption Coefficients, Frontiers in Marine Science, 3, https://doi.org/10.3389/fmars.2016.00007, http://journal.frontiersin.org/Article/10.3389/fmars.2016.00007/abstract, 2016.

Forest, A., Babin, M., Stemmann, L., Picheral, M., Sampei, M., Fortier, L., Gratton, Y., Bélanger, S., Devred, E., Sahlin, J., Doxaran, D., Joux, F., Ortega-Retuerta, E., Martín, J., Jeffrey, W. H., Gasser, B., and Carlos Miquel, J.: Ecosystem function and particle flux dynamics across the Mackenzie Shelf (Beaufort Sea, Arctic Ocean): an integrative analysis of spatial variability and biophysical forcings, Biogeosciences, 10, 2833–2866, https://doi.org/10.5194/bg-10-2833-2013, www.biogeosciences.net/10/2833/2013/https://www.biogeosciences.net/10/2833/2013/, 2013.

Galeron, M.-A., Radakovitch, O., Charrière, B., Vaultier, F., Volkman, J. K., Bianchi, T. S., Ward, N. D., Medeiros, P. M., Sawakuchi,
515   H. O., Tank, S., Kerhervé, P., and Rontani, J.-F.: Lipoxygenase-induced autoxidative degradation of terrestrial particulate or-
       ganic matter in estuaries: A widespread process enhanced at high and low latitude, Organic Geochemistry, 115, 78–92,
       https://doi.org/10.1016/j.orggeochem.2017.10.013, https://linkinghub.elsevier.com/retrieve/pii/S0146638017303868, 2018.

Guillot, P. and Gratton, Y.: Malina 0902 CTD Processing Notes. Quebec Ocean internal report., Tech. rep., Rimouski, Qc., 2010.

Holmes, R. M., Aminot, A., Kérouel, R., Hooker, B. A., and Peterson, B. J.: A simple and precise method for measuring
520   ammonium in marine and freshwater ecosystems, Canadian Journal of Fisheries and Aquatic Sciences, 56, 1801–1808,
       https://doi.org/10.1139/f99-128, http://www.nrcresearchpress.com/doi/10.1139/f99-128, 1999.

Hooker, S. B., Morrow, J. H., and Matsuoka, A.: Apparent optical properties of the Canadian Beaufort Sea – Part 2: The
       1and validating AOP data products, Biogeosciences, 10, 4511–4527, https://doi.org/10.5194/bg-10-4511-2013, https://www.
       biogeosciences.net/10/4511/2013/, 2013.

525 Kaiser, K. and Benner, R.: Hydrolysis-induced racemization of amino acids, Limnology and Oceanography: Methods, 3, 318–325,
       https://doi.org/10.4319/lom.2005.3.318, http://doi.wiley.com/10.4319/lom.2005.3.318, 2005.

Kirchman, D. L., Morán, X. A. G., and Ducklow, H.: Microbial growth in the polar oceans — role of temperature and potential impact
       of climate change, Nature Reviews Microbiology, 7, 451–459, https://doi.org/10.1038/nrmicro2115, http://www.nature.com/
       articles/nrmicro2115, 2009.

530 Kirkwood, D.: Stability of solutions of nutrient salts during storage, Marine Chemistry, 38, 151–164, https://doi.org/10.1016/0304-
       4203(92)90032-6, https://linkinghub.elsevier.com/retrieve/pii/0304420392900326, 1992.

Lansard, B., Mucci, A., Miller, L. A., Macdonald, R. W., and Gratton, Y.: Seasonal variability of water mass distribution in the
       southeastern Beaufort Sea determined by total alkalinity and δ18 O, Journal of Geophysical Research: Oceans, 117, n/a–n/a,
       https://doi.org/10.1029/2011JC007299, http://doi.wiley.com/10.1029/2011JC007299, 2012.

535 Le Fouest, V., Zakardjian, B., Xie, H., Raimbault, P., Joux, F., and Babin, M.: Modeling plankton ecosystem functioning and nitrogen
       fluxes in the oligotrophic waters of the Beaufort Sea, Arctic Ocean: a focus on light-driven processes, Biogeosciences, 10,
       4785–4800, https://doi.org/10.5194/bg-10-4785-2013, https://www.biogeosciences.net/10/4785/2013/, 2013.

Link, H., Chaillou, G., Forest, A., Piepenburg, D., and Archambault, P.: Multivariate benthic ecosystem functioning in the
       Arctic – benthic fluxes explained by environmental parameters in the southeastern Beaufort Sea, Biogeosciences, 10,
540   5911–5929, https://doi.org/10.5194/bg-10-5911-2013, https://www.biogeosciences.net/10/5911/2013/https://bg.copernicus.
       org/articles/10/5911/2013/, 2013.

Louchouarn, P., Opsahl, S., and Benner, R.: Isolation and Quantification of Dissolved Lignin from Natural Waters Using Solid-
       Phase Extraction and GC/MS, Analytical Chemistry, 72, 2780–2787, https://doi.org/10.1021/ac9912552, https://pubs.acs.org/
       doi/10.1021/ac9912552, 2000.

545 Macdonald, R. W., Carmack, E. C., McLaughlin, F. A., Iseki, K., Macdonald, D. M., and O'Brien, M. C.: Composition
       and modification of water masses in the Mackenzie shelf estuary, Journal of Geophysical Research, 94, 18 057,
       https://doi.org/10.1029/JC094iC12p18057, http://doi.wiley.com/10.1029/JC094iC12p18057, 1989.

Marchand, D. and Rontani, J.-F.: Characterisation of photo-oxidation and autoxidation products of phytoplanktonic mo-
       nounsaturated fatty acids in marine particulate matter and recent sediments, Organic Geochemistry, 32, 287–304,
550   https://doi.org/10.1016/S0146-6380(00)00175-3, https://linkinghub.elsevier.com/retrieve/pii/S0146638000001753, 2001.

Marie, D., Brussaard, C. P. D., Partensky, F., and Vaulot, D.: Flow cytometric analysis of phytoplankton, bacteria and viruses, in: Current protocols in cytometry, edited by Robinson, J. P., vol. 11.11, pp. 1–15, John Wiley & Sons, New York, 1999.

Massicotte, P., Asmala, E., Stedmon, C., and Markager, S.: Global distribution of dissolved organic matter along the aquatic continuum: Across rivers, lakes and oceans, Science of The Total Environment, 609, 180–191, https://doi.org/10.1016/j.scitotenv.2017.07.076, http://linkinghub.elsevier.com/retrieve/pii/S0048969717317783, 2017.

Massicotte, P., Amon, R., Antoine, D., Archambault, P., Balzano, S., Bélanger, S., Benner, R., Boeuf, D., Bricaud, A., Bruyant, F., Chaillou, G., Chami, M., Charrière, B., Chen, J., Claustre, H., Coupel, P., Delsaut, N., Doxaran, D., Ehn, J., Fichot, C., Forget, M.-H., Fu, P., Gagnon, J., Garcia, N., Gasser, B., Ghiglione, J.-F., Gorsky, G., Gosselin, M., Gourvil, P., Gratton, Y., Guillot, P., Heipieper, H. J., Heussner, S., Hooker, S., Huot, Y., Jacq, V., Jeanthon, C., Jeffrey, W., Joux, F., Kawamura, K., Lansard, B., Leymarie, E., Link, H., Lovejoy, C., Marec, C., Marie, D., Martin, J., Massé, G., Matsuoka, A., McKague, V., Mignot, A., Miller, W. L., Miquel, J.-C., Mucci, A., Ono, K., Ortega, E., Panagiotopoulos, C., Papakyriakou, T., Para, J., Picheral, M., Piepenburg, D., Prieur, L., Raimbault, P., Ras, J., Reynolds, R. A., Rochon, A., Rontani, J.-F., Schmechtig, C., Schmidt, S., Sempéré, R., Shen, Y., Song, G., Stramski, D., Stroud G., D., Tachibana, E., Thirouard, A., Tolosa, I., Tremblay, J.-É., Vaïtilingom, M., Vaulot, D., Vaultier, F., Volkman, J. K., Vonk, J. E., Xie, H., Zheng, G., and Babin, M.: The Malina oceanographic expedition: How do changes in ice cover, permafrost and UV radiation impact on biodiversity and biogeochemical fluxes in the Arctic Ocean?, https://doi.org/10.17882/75345, https://www.seanoe.org/data/00641/75345/, 2020.

Matsuoka, A., Bricaud, A., Benner, R., Para, J., Sempéré, R., Prieur, L., Bélanger, S., and Babin, M.: Tracing the transport of colored dissolved organic matter in water masses of the Southern Beaufort Sea: relationship with hydrographic characteristics, Biogeosciences, 9, 925–940, https://doi.org/10.5194/bg-9-925-2012, https://www.biogeosciences.net/9/925/2012/, 2012.

Miller, W. L. and Zepp, R. G.: Photochemical production of dissolved inorganic carbon from terrestrial organic matter: Significance to the oceanic organic carbon cycle, Geophysical Research Letters, 22, 417–420, https://doi.org/10.1029/94GL03344, http://doi.wiley.com/10.1029/94GL03344, 1995.

Morales-Sánchez, D., Schulze, P. S., Kiron, V., and Wijffels, R. H.: Production of carbohydrates, lipids and polyunsaturated fatty acids (PUFA) by the polar marine microalga Chlamydomonas malina RCC2488, Algal Research, 50, 102 016, https://doi.org/10.1016/j.algal.2020.102016, https://linkinghub.elsevier.com/retrieve/pii/S2211926420303477, 2020.

Morel, A.: Optical properties of pure water and pure sea water, in: Optical Aspects of Oceanography, edited by Jerlov, N. and Nielsen, E. S., chap. 1, pp. 1–24, Academic Press, New York, 1974.

Ortega-Retuerta, E., Jeffrey, W. H., Babin, M., Bélanger, S., Benner, R., Marie, D., Matsuoka, A., Raimbault, P., and Joux, F.: Carbon fluxes in the Canadian Arctic: patterns and drivers of bacterial abundance, production and respiration on the Beaufort Sea margin, Biogeosciences, 9, 3679–3692, https://doi.org/10.5194/bg-9-3679-2012, https://www.biogeosciences.net/9/3679/2012/http://www.biogeosciences.net/9/3679/2012/, 2012a.

Ortega-Retuerta, E., Jeffrey, W. H., Ghiglione, J. F., and Joux, F.: Evidence of heterotrophic prokaryotic activity limitation by nitrogen in the Western Arctic Ocean during summer, Polar Biology, 35, 785–794, https://doi.org/10.1007/s00300-011-1109-8, http://link.springer.com/10.1007/s00300-011-1109-8, 2012b.

Ortega-Retuerta, E., Joux, F., Jeffrey, W. H., and Ghiglione, J. F.: Spatial variability of particle-attached and free-living bacterial diversity in surface waters from the Mackenzie River to the Beaufort Sea (Canadian Arctic), Biogeosciences, 10, 2747–2759, https://doi.org/10.5194/bg-10-2747-2013, https://www.biogeosciences.net/10/2747/2013/, 2013.

Percopo, I., Ruggiero, M. V., Balzano, S., Gourvil, P., Lundholm, N., Siano, R., Tammilehto, A., Vaulot, D., and Sarno, D.: Pseudo-nitzschia arctica sp. nov., a new cold-water cryptic Pseudo-nitzschia species within the P. pseudodelicatissima complex, Journal
590   of Phycology, 52, 184–199, https://doi.org/10.1111/jpy.12395, http://doi.wiley.com/10.1111/jpy.12395, 2016.

Raimbault, P. and Garcia, N.: Evidence for efficient regenerated production and dinitrogen fixation in nitrogen-deficient waters of the South Pacific Ocean: impact on new and export production estimates, Biogeosciences, 5, 323–338, https://doi.org/10.5194/bg-5-323-2008, https://www.biogeosciences.net/5/323/2008/, 2008.

Raimbault, P., Slawyk, G., Coste, B., and Fry, J.: Feasibility of using an automated colorimetric procedure for the determi-
595   nation of seawater nitrate in the 0 to 100 nM range: Examples from field and culture, Marine Biology, 104, 347–351, https://doi.org/10.1007/BF01313277, http://link.springer.com/10.1007/BF01313277, 1990.

Raimbault, P., Pouvesle, W., Diaz, F., Garcia, N., and Sempéré, R.: Wet-oxidation and automated colorimetry for simultane-ous determination of organic carbon, nitrogen and phosphorus dissolved in seawater, Marine Chemistry, 66, 161–169, https://doi.org/10.1016/S0304-4203(99)00038-9, https://linkinghub.elsevier.com/retrieve/pii/S0304420399000389, 1999a.

600   Raimbault, P., Slawyk, G., Boudjellal, B., Coatanoan, C., Conan, P., Coste, B., Garcia, N., Moutin, T., and Pujo-Pay, M.: Carbon and nitrogen uptake and export in the equatorial Pacific at 150°W: Evidence of an efficient regenerated production cycle, Jour-nal of Geophysical Research: Oceans, 104, 3341–3356, https://doi.org/10.1029/1998JC900004, http://doi.wiley.com/10.1029/1998JC900004, 1999b.

Ras, J., Claustre, H., and Uitz, J.: Spatial variability of phytoplankton pigment distributions in the Subtropical South Pacific Ocean:
605   comparison between in situ and predicted data, Biogeosciences, 5, 353–369, https://doi.org/10.5194/bg-5-353-2008, http://www.biogeosciences.net/5/353/2008/https://www.biogeosciences.net/5/353/2008/, 2008.

Raymond, P. A., McClelland, J. W., Holmes, R. M., Zhulidov, A. V., Mull, K., Peterson, B. J., Striegl, R. G., Aiken, G. R., and Gurtovaya, T. Y.: Flux and age of dissolved organic carbon exported to the Arctic Ocean: A carbon isotopic study of the five largest arc-tic rivers, Global Biogeochemical Cycles, 21, n/a–n/a, https://doi.org/10.1029/2007GB002934, http://doi.wiley.com/10.1029/
610   2007GB002934, 2007.

Rontani, J. F., Charriere, B., Forest, A., Heussner, S., Vaultier, F., Petit, M., Delsaut, N., Fortier, L., and Sempéré, R.: Intense photoox-idative degradation of planktonic and bacterial lipids in sinking particles collected with sediment traps across the Canadian Beaufort Shelf (Arctic Ocean), Biogeosciences, https://doi.org/10.5194/bg-9-4787-2012, 2012.

Rontani, J.-F., Charrière, B., Sempéré, R., Doxaran, D., Vaultier, F., Vonk, J. E., and Volkman, J. K.: Degradation of sterols
615   and terrigenous organic matter in waters of the Mackenzie Shelf, Canadian Arctic, Organic Geochemistry, 75, 61–73, https://doi.org/10.1016/j.orggeochem.2014.06.002, https://linkinghub.elsevier.com/retrieve/pii/S0146638014001521, 2014.

Röttgers, R. and Gehnke, S.: Measurement of light absorption by aquatic particles: improvement of the quantitative filter technique by use of an integrating sphere approach, Applied Optics, 51, 1336, https://doi.org/10.1364/AO.51.001336, https://www.osapublishing.org/abstract.cfm?URI=ao-51-9-1336, 2012.

620   Shen, Y., Fichot, C. G., and Benner, R.: Dissolved organic matter composition and bioavailability reflect ecosystem produc-tivity in the Western Arctic Ocean, Biogeosciences, 9, 4993–5005, https://doi.org/10.5194/bg-9-4993-2012, https://www.biogeosciences.net/9/4993/2012/, 2012.

Song, G., Xie, H., Bélanger, S., Leymarie, E., and Babin, M.: Spectrally resolved efficiencies of carbon monoxide (CO) photopro-duction in the western Canadian Arctic: particles versus solutes, Biogeosciences, 10, 3731–3748, https://doi.org/10.5194/bg-
625   10-3731-2013, https://www.biogeosciences.net/10/3731/2013/, 2013.

Stein, R. and Macdonald, R. W.: Organic Carbon Budget: Arctic Ocean vs. Global Ocean, in: The Organic Carbon Cycle in the Arctic Ocean, edited by Stein, R. and MacDonald, R. W., pp. 315–322, Springer Berlin Heidelberg, Berlin, Heidelberg, https://doi.org/10.1007/978-3-642-18912-8_8, https://doi.org/10.1007/978-3-642-18912-8_8, 2004.

Taalba, A., Xie, H., Scarratt, M. G., Bélanger, S., and Levasseur, M.: Photooxidation of dimethylsulfide (DMS) in the Canadian
630   Arctic, Biogeosciences, 10, 6793–6806, https://doi.org/10.5194/bg-10-6793-2013, https://www.biogeosciences.net/10/6793/2013/, 2013.

Tank, S. E., Striegl, R. G., McClelland, J. W., and Kokelj, S. V.: Multi-decadal increases in dissolved organic carbon and alkalinity flux from the Mackenzie drainage basin to the Arctic Ocean, Environmental Research Letters, 11, 054 015, https://doi.org/10.1088/1748-9326/11/5/054015, https://iopscience.iop.org/article/10.1088/1748-9326/11/5/054015, 2016.

635 Tremblay, J.-É., Raimbault, P., Garcia, N., Lansard, B., Babin, M., and Gagnon, J.: Impact of river discharge, upwelling and vertical mixing on the nutrient loading and productivity of the Canadian Beaufort Shelf, Biogeosciences, 11, 4853–4868, https://doi.org/10.5194/bg-11-4853-2014, https://www.biogeosciences.net/11/4853/2014/, 2014.

Visbeck, M.: Deep Velocity Profiling Using Lowered Acoustic Doppler Current Profilers: Bottom Track and Inverse Solutions*, Journal of Atmospheric and Oceanic Technology, 19, 794–807, https://doi.org/10.1175/1520-
640   0426(2002)019<0794:DVPULA>2.0.CO;2, http://journals.ametsoc.org/doi/abs/10.1175/1520-0426%282002%29019%3C0794%3ADVPULA%3E2.0.CO%3B2, 2002.

Weishaar, J. L., Aiken, G. R., Bergamaschi, B. A., Fram, M. S., Fujii, R., and Mopper, K.: Evaluation of Specific Ultraviolet Absorbance as an Indicator of the Chemical Composition and Reactivity of Dissolved Organic Carbon, Environmental Science and Technology, 37, 4702–4708, https://doi.org/10.1021/es030360x, https://pubs.acs.org/doi/10.1021/es030360x, 2003.

645 Westerhoff, P., Chao, P., and Mash, H.: Reactivity of natural organic matter with aqueous chlorine and bromine, Water Research, 38, 1502–1513, https://doi.org/10.1016/j.watres.2003.12.014, http://linkinghub.elsevier.com/retrieve/pii/S0043135403006845, 2004.

Xie, H., Bélanger, S., Demers, S., Vincent, W. F., and Papakyriakou, T. N.: Photobiogeochemical cycling of carbon monoxide in the southeastern Beaufort Sea in spring and autumn, Limnology and Oceanography, 54, 234–249,
650   https://doi.org/10.4319/lo.2009.54.1.0234, http://doi.wiley.com/10.4319/lo.2009.54.1.0234, 2009.

Xie, H., Bélanger, S., Song, G., Benner, R., Taalba, A., Blais, M., Tremblay, J.-É., and Babin, M.: Photoproduction of ammonium in the southeastern Beaufort Sea and its biogeochemical implications, Biogeosciences, 9, 3047–3061, https://doi.org/10.5194/bg-9-3047-2012, https://www.biogeosciences.net/9/3047/2012/, 2012.

Yau, S., Lopes dos Santos, A., Eikrem, W., Gérikas Ribeiro, C., Gourvil, P., Balzano, S., Escande, M.-L., Moreau, H., and Vaulot,
655   D.: Mantoniella beaufortii and Mantoniella baffinensis sp. nov. (Mamiellales, Mamiellophyceae), two new green algal species from the high arctic 1, Journal of Phycology, 56, 37–51, https://doi.org/10.1111/jpy.12932, https://www.biorxiv.org/content/early/2018/12/27/506915https://onlinelibrary.wiley.com/doi/abs/10.1111/jpy.12932, 2020.